HHS Public Access

Author manuscript

Cell Rep. Author manuscript; available in PMC 2024 February 20.

Published in final edited form as:

Cell Rep. 2024 January 23; 43(1): 113635. doi:10.1016/j.celrep.2023.113635.

Embryonic temporal–spatial delineation of excitatory spinal V3 interneuron diversity

Dylan Deska-Gauthier[1,4], **Joanna Borowska-Fielding**[1], **Chris Jones**[2], **Han Zhang**[1,5], **Colin S. MacKay**[1], **Ramez Michail**[1], **Laura A. Bennett**[1,4], **Jay B. Bikoff**[3], **Ying Zhang**[1,*]

[1]Department of Medical Neuroscience, Faculty of Medicine, Dalhousie University, Halifax, Nova Scotia, Canada B3H 4R2

[2]Department of Biochemistry and Molecular Biology, Faculty of medicine, Dalhousie University, Halifax, Nova Scotia, Canada B3H 4R2

[3]Department of Developmental Neurobiology, St. Jude Children's Research Hospital, Memphis, Tennessee 38105, USA

[4]Current affiliation: Faculty of Medicine, University of Toronto, Toronto, Ontario, Canada

[5]Current affiliation: Neuroscience and Mental Health Institute and Faculty of Rehabilitation Medicine, University of Alberta, Edmonton, Alberta, Canada.

Summary

Spinal neural circuits that execute movement are comprised of cardinal classes of neurons emerged from distinct progenitor lineages. Each cardinal class contains multiple neuronal subtypes characterized by distinct molecular, anatomical and physiological characteristics. Through a focus on the excitatory V3 interneuron class, here we demonstrate that interneuron subtype diversity is delineated through a combination of neurogenesis timing and final laminar settling position. We have revealed that early-born or late-born embryonic V3 temporal classes further diversify into subclasses with spatially and molecularly discrete identities. While neurogenesis timing account for V3 morphological diversification, laminar settling position account for electrophysiological profiles distinguishing V3 subtypes within the same temporal classes. Furthermore, V3 IN subtypes display independent behavioural recruitment patterns demonstrating a functional modularity underlying V3 interneuron diversity. These studies provide a framework for how early embryonic temporal and spatial mechanisms combine to delineate interneuron classes into molecularly, anatomically, and functionally relevant subtypes in adults.

*Corresponding Author and Lead Contact: Ying.Zhang@dal.ca.

Author Contributions

Conceptualization, D.D.G. and Y.Z.; Main methodology; Data collection and analysis, mainly by D.D.G. and J.B.F, assisted by H.Z., C.S.M., R.M. and L.A.B; Computational model, C.J.; resources, J.B.B; writing and figure generation – original draft, D.D.G.; writing – review & editing, D.D.G., Y.Z. and J.B.B; all authors reviewed, edited, or commented on the manuscript; supervision and funding acquisition, Y.Z.

Declaration of Interests

The authors declare no competing interests.

Introduction

Neuronal circuits in the spinal cord directly control the coordination, precision, and adaptability of movement. Such extensive feats of sensorimotor control are hypothesized to be achieved through the vast diversity of molecularly, anatomically, morphologically, and physiologically distinct interneuron (IN) types in the spinal[1,2]. Spinal IN types assemble into unique circuit arrangements during early development enabling dynamic speed-, sensory-, and balance-dependent sensorimotor control throughout maturation and adulthood[3].

Spinal IN diversification begins during early embryogenesis. Opposing morphogen gradients establish 11 progenitor domains that give rise to discrete post-mitotic cardinal IN classes and motor neurons[4]. While neurons within each cardinal IN class share early developmental origins and molecular signatures, each class further displays functional[2,5,6] and molecular[7,8] subtype divergence by postnatal stages. Particularly, recent transcriptomic studies have revealed immense transcription factor networks diversifying spinal neuron molecular clusters well beyond their 11 progenitor domains of origin[9–17].

To what extent intraclass molecular heterogeneity between INs from a shared progenitor domain translates into meaningful circuit diversity remains a largely unanswered and crucial question. Matching the molecular subtypes within cardinal classes to functional circuit arrangements is a vital next step towards ultimately understanding how the spinal cord achieves complex and nuanced states of sensorimotor control. Here, we address these issues through an examination of the developmental mechanisms linking molecular specification to circuit organization of subtypes within the spinal V3 IN class.

The cardinal V3 IN class is defined by post-mitotic expression of the Sim1 transcription factor. As a major group of excitatory spinal INs, V3 INs are crucial in regulating motor output[18] and are necessary for the generation of robust and coordinated locomotor activities across different speeds[19,20]. Furthermore, recent studies indicate that V3 INs mediate sensory-afferent evoked muscle spasms post-spinal cord injury, suggesting they may also play crucial pathophysiological roles in injury and disease states[21].

Despite arising from a shared spatially and molecularly confined progenitor domain[20], V3 INs are highly heterogenous[19,20,22–24]. Until now, however, we have not been able to define V3 subtype identities. This has presented major hurdles when attempting to match V3 circuit connectivity to functional outputs and pathophysiological states.

To overcome this hurdle, in our current work, we have first identified five transcription factors (TFs) as molecular markers of spatially separated V3 IN subsets and demonstrate that these V3 IN subtypes emerge during early- or late-born neurogenesis windows. Utilizing these molecular markers, we then further uncover the early developmental logic giving rise to distinct V3 IN subtypes by postnatal stages. We reveal that a combination of neurogenesis timing and final spatial positioning diversifies distinct V3 IN subtype axon projection profiles, morphologies and electrophysiologic properties. However, temporal and spatial factors appear to play separate roles in their unique differentiation trajectories. Neurogenesis timing is associated with V3 morphological diversification while laminar settling position is associated with V3 electrophysiological diversification. More

importantly, we demonstrate in the mature spinal cord that distinct V3 IN molecular subtypes display overlapping, yet independent, task-specific recruitment patterns. Thus, our current work provides a framework for how early embryonic temporal and spatial mechanisms combine to delineate spinal INs into molecularly, anatomically and functionally diverse subtypes by postnatal stages.

Results

Topographically clustered V3 INs display unique transcription factor expression profiles

We first aimed to identify candidate molecular markers expressed in spatially separated clusters of postnatal V3 INs. Taking advantage of recent molecular and single cell sequencing studies characterizing spinal IN diversity[12,14,25,26], we focused on a small cohort of TFs and identified five – Olig3, Pou2f2, Nr3b3, Onecut2 and Prox1 – that displayed distinct expression patterns within spatially clustered V3 IN subsets throughout rostral lumbar (L1-L3) spinal cord segments of postnatal day (P) 0 *Sim1*^{Cre}*;Rosa.lsl.tdTom* mice (Figure1A–D; Supplemental Figure1). Among them, Olig3^{+} V3 INs clustered within the ventral spinal cord (Figure1E); Nr3b3^{+} V3 INs formed a predominantly dorsomedial cluster within laminae V with some ventral clustering in laminae XIII (Figure1F); and Prox1^{+}, Pou2f2^{+} and Onecut2^{+} V3 INs clustered in more intermediate positions within laminae VI, VII, and X (Figure1G–I). In total these molecularly and spatially distinguishable V3 IN subtypes (Figure1J) accounted for approximately 70% of all V3 INs within the neonatal rostral lumbar (L1-L3) spinal cord (Figure1K).

To determine whether these TFs define non-overlapping subsets of V3 INs, we next examined the potential combinatorial expressions of Olig3, Pou2f2, Nr3b3, Onecut2 and Prox1 within single spatially-defined V3 INs. We performed immunohistochemical analyses across all possible pairwise TF combinations (Supplemental Figure2). Interestingly, of all TF combinations, only two pairs displayed notable spatial and molecular overlap: (1) Pou2f2 and Onecut2 (Figure1L, Supplemental Figure2H), and (2) Olig3 and Prox1 (Figure1L, Supplemental Figure2D). These results are particularly interesting as recent transcriptome data revealed Pou2f2 and Onecut2 are markers of early-born spinal INs[12], whereas Prox1 marks later-born spinal INs[15], suggesting that neurogenesis timing may be a key determinant of V3 molecular subtype identity.

Molecularly and spatially distinct V3 INs emerge during early- or late-born neurogenesis windows

To explore whether distinct subsets of V3 INs can be distinguished by timing of neurogenesis, we took advantage of two complementary approaches to fate-map V3 INs; employing intersectional and inducible transgenic mouse lines as well as injecting timed pregnant mice with the thymidine analog, 5-Ethynyl-2´-deoxyuridine (EdU). We first crossed *Sim1*^{Cre}*;Nestin*^{FlpoER} mice with *Gt(ROSA)26Sor*$^{tm65.1(CAG-tdTomato)Hze}$ (Ai65D) mice containing *tdTomato* downstream of both a *frt*-flanked and a *loxP*-flanked *STOP* cassette (Figure2A). To fate-restrict V3 INs with successive neurogenesis times, we induced Flpo activation via tamoxifen injection at either E10.5, E11.5, or E12.5, respectively, and analyzed V3 diversity at E14.5 (Figure2B) – a time at which V3 INs display a molecular and

spatial organization that is largely indistinguishable to that observed at P0. For comparison, V3 INs born across all times (E9.5-E12.5) were visualized using a *Sim1^{Cre};Rosa.lsl.tdTom* mouse at E14.5 (Figure2C).

With progressive tamoxifen injections at E10.5, E11.5, or E12.5 in *Sim1^{Cre};Nestin^{FlpoER};Ai65D* mice, V3 INs became increasingly fate-restricted to ventral and molecularly distinct subtypes (Figure2D). With each successive tamoxifen induction timepoint, V3 INs displayed a reduced number of Onecut2^{+}, Pou2f2^{+}, and Nr3b3^{+} V3 INs (Figure2E–G). In contrast, the proportion of Olig3^{+} and Prox1^{+} V3 IN subtypes increased with successive tamoxifen induction timepoints until E11.5 and E12.5, respectively (Figure2F).

To further and independently explore neurogenesis timing of V3 IN subsets, we next injected pregnant *Sim1^{Cre};Rosa.lsl.tdTom* mice with EdU at E9.5, E10.5, E11.5, or E12.5 and subsequently performed EdU detection at E14.5 (Figure2H–I). In line with the tamoxifen induction data, Onecut2^{+}, Pou2f2^{+} and Nr3b3^{+} V3 INs all displayed peak EdU detection between E9.5 and E10.5 (Figure2J–K). In contrast, Olig3^{+} and Prox1^{+} V3 INs displayed negligible EdU detection until E11.5. By E12.5, a substantial proportion of Prox1^{+} V3 INs were still detected as well as a smaller subset of ventromedially clustered Olig3^{+} V3 INs (Figure2K).

This raised the question of whether V3 INs originating in the same neurogenesis wave are molecularly discrete from birth or post-mitotically acquire molecular specificity as they spatially separate between E10.5 and E14.5 (Supplemental Figure3). To distinguish between these possibilities, we first investigated the immediate post-mitotic expression profiles of early- or late-born V3 INs, respectively. We performed triple immunohistochemical analyses of Onecut2, Pou2f2 and Nr3b3 V3 expressions between E10.5-E14.5 (Supplemental Figure4A,C,E) or dual immunoreactivity of Olig3 and Prox1 V3 expressions between E12.5-E14.5 in Sim1Cre;Rosa.lsl.tdTom lumbar spinal cords (Supplemental Figure4B,D,F). Interestingly, at E10.5 – prior to forming migratory streams – the majority of early-born V3 INs were molecularly unspecified (Supplemental Figure4E). Indeed, approximately 93% of V3 INs co-expressed Onecut2, Pou2f2 and Nr3b3 at E10.5. As development proceeds between E11.5-E14.5, early-born V3 INs progressively diverged in their molecular and spatial profiles, such that by E14.5 they displayed separation comparable to P0 spinal cords (Supplemental Figure4E). Late-born Olig3^{+} and Prox1^{+} V3 INs were first detected with heightened levels at E12.5 (Supplemental Figure4F) where the majority of Prox1^{+} V3 INs co-expressed Olig3 (>80% at E12.5). However by E14.5, about half of Prox1^{+} V3 INs (54 ± 8%) co-expressed Olig3 (the same ratio observed at P0).

These observations suggested that within respective early- or late-neurogenesis temporal subclasses, V3 IN subtypes became molecularly specified in accordance with their divergent post-mitotic migrations. This raised the intriguing possibility of a hierarchical temporospatial scheme underlying V3 molecular divergence. Indeed, while V3 INs displayed early post-mitotic molecular overlap between neurogenically shared TF identities (early-born or late-born; Supplemental Figure 4), no co-expressions of Olig3 (late-born TF) with either Onecut2 or Pou2f2 (early-born TFs) was detected at E11.5 (Figure3A–B).

Furthermore, the co-expression overlaps observed at P0 between Olig3-Prox1 (Figure3C, Supplemental Figure2D) and Pou2f2-Onecut2 (Figure3D, Supplemental Figure2H) were confined to V3 subsets born within the same neurogenesis windows. In contrast, TFs expressed in spatially overlapping but temporally separated V3 INs (for example, Pou2f2-Olig3, Figure3E, Supplemental Figure2B; Pou2f2-Prox1, Figure3F, Supplemental Figure2I) displayed almost zero co-expression. Thus, Olig3, Pou2f2, Nr3b3, Onecut2 and Prox1 each uniquely defined the spatial-temporal identities of the distinct V3 IN subtypes they were expressed in.

Taken together, V3 INs molecularly diversified along a temporospatial hierarchy during early embryonic development. Along the temporal axis, two major neurogenesis waves delineated an early-born (E9.5-E10.5) V3 cohort marked by Onecut2, Pou2f2, and Nr3b3, and a late-born (E11.5-E12.5) V3 cohort marked by Olig3 and Prox1. Subsequently, within each V3 temporal subclass, post-mitotic early- or late-born V3 INs specified into molecularly distinct or overlapping subtypes in accordance with their final laminar settling positions (Figure3G).

Defining embryonic to postnatal trajectories that organize the functional properties of V3 IN molecular subtypes

Cell-type identification and classification is most powerful when multimodal information is integrated into a coherent framework. Accordingly, we explored whether embryonic V3 molecular subtypes develop divergent intrinsic properties, such as axon projection profiles, dendritic arborizations and electrophysiological parameters. Furthermore, we wished to address whether these V3 subtype parameters emerged from the same early embryonic temporal and spatial mechanisms organizing their molecular identities.

Combinatorial transcription factor expressions delineate V3 IN axonal projection patterns across development—The elaboration and orientation of axonal arborization is a key aspect of neuronal identity and is one of the first properties acquired during post-mitotic development. In the spinal cord, IN axon projection identities have been suggested to emerge in temporally ordered sequences during embryogenesis[27]. V3 INs display heterogenous ascending, descending, commissural and ipsilateral axonal projections[22], providing an ideal system to explore how divergent axonal patterns arise during development. To define the developmental trajectories of V3 IN subtype axon projection profiles, we performed retrograde tract tracing and post-hoc immunolabeling between E11.5 to E14.5 as V3 INs are exiting the p3 progenitor domain and migrating to their final laminar locations (Figure4A–C). The retrograde tracer Biotin-Dextran-Amine (BDA) was injected into one side of the spinal cord at approximately the L1 segment. Cell bodies labeled rostral to the injection site were categorized as descending and those caudal to the injection site as ascending.

We found that V3 molecular subtypes displayed distinct temporal trajectories of their axon projections. At E11.5, almost all descending, ipsilaterally-projecting axons belonged to Onecut2^{+} V3 INs, which remained as the descending ipsilaterally-projecting V3 IN subtype until E14.5 (Figure4D). In contrast, at E11.5 the majority (90 ± 13%,mean ± SD) of

early emerging descending commissural projecting V3 INs were Pou2f2^{+} (Figure4D). Thus, Onecut2 and Pou2f2 delineated the descending axon phenotype of early-born V3 temporal subclasses into either ipsilateral or contralateral identities, respectively.

At E12.5, ascending commissural projecting V3 INs emerged as a mixture of Pou2f2^{+}, Nr3b3^{+}, and Olig3^{+} V3 IN subtypes (Figure4E). While projection profiles of Onecut2^{+}, Pou2f2^{+} and Nr3b3^{+} V3 INs remained relatively unchanged after E12.5, we observed a notable increase in the proportion of Olig3^{+} descending commissural projecting V3 INs at E13.5 (Figure4F), which were maintained throughout subsequent development (Figure4G). Of note, we did not detect any Prox1^{+} V3 axon projections ascending nor descending at these early embryonic stages (E11.5-E13.5), suggesting this V3 subtype may have highly restricted, local axonal arborization patterns emerging at E14.5 (Supplemental Figure5). Thus, in addition to ventromedial fate-restriction, late-born Prox1^{+} V3 IN axon projections were also restricted to contralateral local segments. Taken together, these data indicate that the temporal neurogenesis ordering of V3 molecular diversity coincided with the post-mitotic emergence of subset-specific axon projection profiles across successive timepoints.

We next focused more in depth on the axon projection profiles of V3 IN subtypes at E14.5 – the time point that V3 INs reach their final laminar settling positions and express molecular identities comparable to neonatal stages. Onecut2^{+} V3 INs clustered within laminae VII were almost exclusively descending ipsilateral (Figure4H,L) and comprised almost all descending ipsilateral V3 INs. Though, Pou2f2^{+} V3 INs also displayed descending ipsilateral projections in addition to descending commissural and ascending commissural axon projections (Figure4I,M). Dual retrograde tract tracing experiments confirmed that while a portion of Pou2f2^{+} V3 INs may possess bifurcating axon projections (Supplemental Figure6), the majority exclusively displayed one of the three projection phenotypes. Nr3b3^{+} V3 INs clustered within dorsomedial laminae V exhibited relatively homogenous ascending commissural axon projections (Figure4J,N). In contrast, Olig3^{+} V3 INs clustered in ventral laminae exhibited more heterogeneous commissural axonal patterns, in which ~30% of Olig3^{+} V3 INs were ascending commissural while the remaining 70% were descending commissural (Figure4K,N). We detected no bifurcating commissural ascending and descending V3 axon projections at E14.5 (Supplemental6Ai).

INs projecting between lumbar and cervical spinal cord segments play crucial roles in coordinating quadrupedal locomotion[28]. We recently demonstrated that a subset of lumbar V3 INs project long ascending commissural axons to the cervical spinal cord (V3 aLPNs)[19], raising the question of whether any of our V3 subsets correspond to these lumbar-cervical V3 INs. As both dorsal Nr3b3^{+} and intermediate Pou2f2^{+} V3 INs displayed commissural ascending projections, we next examined whether they projected out of the lumbar spinal cord to cervical spinal segments (Supplemental7). At P21, Nr3b3^{+} V3 INs comprised the majority of lumbar-cervical ascending V3 INs (72.7 ± 1.3 %, Supplemental Figure7Ci,D) while Pou2f2^{+} V3 INs comprised the remainder (18.1 ± 1.3 %, Supplemental Figure7Cii,D). Thus, early-born ascending V3 INs projected out of the lumbar spinal cord to cervical circuits.

The heterogenous projection profiles within the Pou2f2$^+$ and Olig3$^+$ V3 IN subsets raised the possibility that each subset itself contains diverse types of V3 INs. Accordingly, we explored whether V3 projection variations might be delineated by increasingly refined TF expression combinations. We first tested two molecular combinations for Pou2f2$^+$ V3 INs: Pou2f2 + Onecut2 (Supplemental Figure8A); and Pou2f2 + Bhlhb5 (Bhlhb5: a TF marker for ventral spinal neurons[26]; Supplemental Figure1; Supplemental Figure8B). Interestingly, we found that exclusively descending ipsilateral Pou2f2$^+$ V3 INs co-expressed Onecut2, and they clustered uniquely medially compared to the total ipsilaterally projecting Onecut2$^+$ V3 INs. Pou2f2$^+$/Bhlhb5$^+$ V3 INs clustered medially and displayed distinctly ascending commissural axon projections (Supplemental Figure8B). We also tested the combination of Olig3 + Bhlhb5 in V3 INs. The combinatorial TF expression of Olig3 with Bhlhb5 also further spatially confined Olig3$^+$ V3 INs to more ventromedial locations (Supplemental Figured8C). Taken together, these studies demonstrate that V3 molecular subtypes were first organized into temporal classes, which were subsequently refined into spatial and projection-specific subclasses marked by combinatorial expression of TFs emerging in succession between E11.5-E14.5 (Figure4P).

Postnatal V3 IN molecular subtypes possess distinct intrinsic properties corresponding to their embryonic spatial and temporal identities—The electrophysiological and morphological properties of V3 INs, like all other neurons, are continuously shaped during postnatal maturation stages[23,29]. Yet as early as P0, V3 INs oriented along the dorsoventral axis already exhibit a gradient of different intrinsic functional properties[29], suggesting that the embryonic molecular distinctions we have identified amongst V3 INs may reflect important differences in neuronal function. To determine the intrinsic property diversity of embryonically delineated V3 molecular subtypes, we performed whole-cell patch clamp recordings of V3 INs in spinal cord slices between P7-P12. V3 IN molecular identities, spatial positions, and morphologies were determined via post hoc analysis for all major subtypes (Figure5A–D), with the exception of Onecut2, which we could not reliably detect due to diminished Onecut2 immunoreactivity after P5 (data not shown).

We analyzed a full spectrum of V3 electrophysiological and morphological properties (Figure5E–H, Supplemental Figures9–11). Not surprisingly, V3 INs displayed highly varied intrinsic properties. While many properties were statistically different among different V3 subtypes, there was no single electrophysiological nor morphological predictor that fully separated all four subtypes. Thus, we next performed supervised clustering analysis. After iterative rounds of optimization (data not shown), we picked six electrophysiological and four morphological properties as the most significant predictors and conducted principal component analyses (Supplemental Figure11E–R).

To visualize potential clustering, scatter plots of the first two principal components were constructed for the six electrophysiological predictors (Figure5I, Supplemental Figure11E–J) and the four morphological predictors (Figure5J, Supplemental Figure11K–N). Similar to our previous work[23,29], the electrophysiological first principal component (PC1) revealed two general clusters: 1) more dorsal Nr3b3$^+$ and Pou2f2$^+$ V3 INs; and 2) more ventral

Olig3$^+$ and Prox1$^+$ V3 INs (Figure5I). Nr3b3$^+$ and Pou2f2$^+$ V3 INs clustered across positive (>0) PC1 scores while Olig3$^+$ and Prox1$^+$ V3 INs clustered across negative (<0) PC1 scores.

The morphological principal components displayed a somewhat less clear, yet still unique separation pattern (Figure5J). Pou2f2$^+$ V3 INs appeared the most divergent of the four subpopulations along the PC1 axis displaying uniquely large and complex dendritic trees (Supplemental Figure11B). Notably, when we performed PCA combining all six electrophysiological and four morphological properties (Figure5K, Supplemental Figure11O–R), we identified the best separations of V3 molecular subtypes across PC1 and PC2 axes. Thus, combined electrophysiological and morphological parameters most accurately separated molecularly distinct V3 IN subtypes.

To further confirm the accuracy of V3 IN subtype separation using the electrophysiological and morphological predictors, we conducted supervised classification analysis using a support vector machine (SVM) learner. V3 molecular prediction accuracies were obtained based on: 1) only electrophysiological predictors (Figure5L); 2) only morphological predictors (Figure5M); and 3) a combination of both electrophysiological and morphological predictors (Figure5N). All three predictor groups produced accuracies significantly greater than chance, which would produce a prediction accuracy of approximately 25% (1 in 4). The combined predictors produced the highest total prediction accuracy (Figure5N), followed by the electrophysiological predictors (Figure5L), and morphological predictors (Figure5M).

Interestingly, several of the morphological properties displayed a decreasing or increasing trend aligned with the neurogenesis times of their respective V3 IN subtypes. This raised the possibility that in addition to spatial positioning, early embryonic neurogenesis timing could be a determining factor for V3 IN intrinsic properties. To test this hypothesis, we recorded V3 INs born at different neurogenesis time points labeled with EdU injected at E10.5, E11.5, or E12.5, respectively (Figure6A–C). To eliminate potential confounding spatial separation, we targeted V3 INs selectively within ventral laminae across all three neurogenesis time points (Figure6D, Supplemental Figure12A–C).

We examined the same 6 electrophysiological properties and the 4 morphological properties previously identified (Figure6E–G, Supplemental Figure12D–M). Of the six electrophysiologic properties, 3 (capacitance, action potential threshold, F-I linear first spike frequency) were statistically different between E10.5 EdU$^+$ V3 INs and later born V3 INs (Figure6H–I, Supplemental Figure12D–I). In contrast, sag amplitude, rheobase spike latency, and afterhyperpolarization were not significant across V3 neurogenesis times (Figure6J–K, Supplemental FIgure12D–I), though, they accounted for large portions of the variance between the molecularly and spatially distinct V3 IN subtypes.

Interestingly, the temporally changed electrophysiological properties were related to neuronal surface size. Indeed, for morphological analyses, total dendritic intercepts (from 0–100μm diameter from soma), maximum dendritic intercepts, and cell body volumes were the significantly largest in E10.5 EdU$^+$ V3 INs (Figure6L–M, Supplemental Figure12J–M). These results reflect a trend of morphologies becoming less elaborate in later-born V3 IN subtypes compared with early born V3 INs.

Taken together, V3 electrophysiological properties separated along a spatial anatomical axis while V3 morphological properties separated along a temporal neurogenesis axis. When combined, spatiotemporal parameters were sufficient to produce molecularly, electrophysiologically, and morphologically distinct V3 IN subpopulations in the postnatal spinal cord.

Prox1$^+$ and Pou2f2$^+$ V3 IN subtypes display overlapping, yet independent, sensorimotor recruitment patterns

Spinal IN networks consist of modular circuits recruited across distinct sensorimotor tasks[3,30]. Our current work suggests that neurogenesis timing combined with spatial positioning may delineate V3 INs into functionally distinct circuits. Prox1$^+$ and Pou2f2$^+$ V3 INs form spatially overlapping, yet temporally distinct, V3 IN subpopulations. To our advantage, Prox1 and Pou2f2 expressions were maintained and detectable in the adult mouse spinal cord, enabling an investigation of task-specific recruitment patterns of Prox1$^+$ and Pou2f2$^+$ V3 INs. Accordingly, we subjected adult mice (>P21) to a specific behavioural task followed by post hoc c-fos detection (Figure7A–B, Supplemental Figure 13). Prior to tissue extraction, mice performed one of six tasks: flat treadmill locomotion at a slow (15cm/s) or intermediate (40cm/s) speed (Figure7C–D); free swimming (Figure7E); incline treadmill locomotion (Figure7F); staggered stepping locomotion (Figure7G); or lateral motion without forward stepping (Figure7H).

Pou2f2$^+$ V3 INs displayed relatively heightened levels of c-fos expression across all six behavioural tasks performed (Figure7I). In contrast, Prox1$^+$ V3 INs only displayed heightened levels of c-fos expression following three of the six behaviours (incline locomotion, staggered stepping, and lateral motion; Figure7I). Prox1$^+$ V3 INs displayed negligible c-fos expression following low speed, intermediate speed, and swimming locomotion. Intriguingly, these observations suggest that Prox1$^+$ and Pou2f2$^+$ V3 INs were integrated into functionally distinct spinal circuit organizations – even though they were in overlapping spatial positions – likely owed to their different neurogenesis timings.

Discussion

Molecular diversity and multimodal classification of spinal V3 IN subtypes

Identification of meaningful neuronal types has been one of the most challenging tasks facing neuroscientists since distinct neuronal morphologies were first described by Ramon Y Cajal. The current consensus in the community is to define neuronal types by combing multi-modular approaches; molecular, morphological, anatomical, and electrophysiological profiles[31]. In laminar central nervous system structures, the first factor in considering neuronal type diversity is spatial location due to clear location-function correlations. However, it has been very difficult to use spatial location in the ventral spinal cord as spinal laminar divisions are not so clearly defined as they are in the cerebral cortex or spinal dorsal horn.

Taking a different approach, in the last three decades researchers have grouped ventral spinal neurons into cardinal classes according to their developmental origins and molecular

signatures. This classification approach has revealed crucial circuit elements and principles in sensorimotor control[2,3,5]. Though, fast-evolving gene sequencing technologies have revealed unexpected molecular diversities within spinal IN classes imposing further unprecedented challenges to delineating functionally meaningful spinal cord IN diversity.

In the current study, we surveyed candidate TFs identified by various sequencing and screening studies in spinal INs[12,14,15,25,26]. We found that most of these TFs were expressed indistinctly across V3 spatial subsets. Only five TFs (Onecut2, Pou2f2, Nr3b3, Olig3, and Prox1) were expressed in subsets of V3 INs with relatively well-defined spatial boundaries in late embryonic and neonatal spinal cords. Interestingly, two of these molecular subsets, $Nr3b3^+$ and $Olig3^+$ V3 INs, directly corresponded to the dorsal and ventral V3 clusters we physiologically described in our previous studies[23,29], respectively. In contrast, $Pou2f2^+$, $Prox1^+$ and $Onecut2^+$ V3 INs clustered in well-bordered but somewhat overlapping territories in the intermediate-ventromedial regions.

Of particular interest, the spatially overlapping $Pou2f2^+$ and $Prox1^+$ V3 subpopulations possessed substantially distinct intrinsic properties and axon projection profiles. Thus, in the ventral spinal cord, while spatial separation has been demonstrated to play important roles in organizing IN subtypes, it is not necessarily sufficient to organize distinctions between molecular IN subsets. This was also demonstrated with V2a IN subtypes in the adult zebrafish spinal cord, which form unique circuit connectivities and contribute to distinct locomotor frequencies[32], yet are completely spatially overlapping.

Thus, it may not be surprising that our current work confirmed that combined molecular, anatomical, electrophysiological, and morphological investigations were required to determine V3 IN subpopulation diversities. This step forward makes V3 INs an ideal model system for addressing how developmental trajectories construct functionally distinct spinal IN subpopulations utilized across varied forms of locomotion.

V3 IN molecular diversity is delineated through a combination of neurogenesis timing and final laminar settling position

Early embryonic neurogenesis timing provides key information required to explain the delineation of spinal IN diversity[33]. In the mouse spinal cord, single cell sequencing across early embryonic stages revealed a temporal emergence of post-mitotic clades spanning cardinal spinal IN classes[12]. Perhaps the best example for such precisely timed neurogenesis is Renshaw Cells (RCs). RC specific TFs were present in the first emerging V1 IN clade[12]. These findings aligned with previous work identifying RCs as the first V1 IN subpopulation to exit from the p1 progenitor domain before migrating ventrolaterally and forming a recurrent inhibitory feedback loop with motor neurons[34,35]. Furthermore, by combining single cell sequencing with anatomical investigations, Osseward and colleagues[15] recently categorized ventral cardinal IN classes into molecular subsets corresponding to distinct medial-lateral locations, axon projection ranges and neurogenesis timings.

In our own previous study, we demonstrated that neurogenesis timing separates V3 INs into either early-born or late-born anatomical distributions. Earlier born V3 INs distributed across dorsoventral and mediolateral axes, while later born V3 INs were restricted to more

ventral and medial regions[36]. Here, we further identified 3 early- (Onecut2$^+$, Pou2f2$^+$ and Nr3b3$^+$) and 2 later-born (Olig3$^+$ and Prox1$^+$) V3 IN subtypes expressing distinct TFs. Several of these TFs, Onecut2 and Pou2f2, have been suggested to serve as molecular temporal codes delineating neuronal diversity across central nervous system (Sagner et al 2021). Similar to our current work, Sagner and colleagues[37] showed Onecut2 expressed in early-born neuronal subtypes followed closely by Pou2f2 in intermediate-born neuronal subtypes.

In the spinal cord, Onecut2, Pou2f2 and Prox1 have been shown to delineate the molecular-temporal identifies of spinal neurons across cardinal IN classes[12,15,37]. Though, Olig3 and Nr3b3 have not been identified as general temporal codes shared across the central nervous system or spinal cord. Indeed, Olig3 appears to have more selective expression confined to the most dorsal or most ventral spinal interneuron classes[12]. Thus, the TFs we have uncovered here delineating V3 INs may result from a combination of both general and class-specific temporal-spatial TF expressions.

Our current study showed that V3 molecular subtypes from different neurogenesis groups often shared overlapping spatial locations without molecular overlap. Furthermore, molecularly distinct V3 IN subtypes with a shared neurogenesis group were often spatially separated. These studies suggest a general logic for spinal interneuron heterogeneity, in which timing of neurogenesis serves as the first organizing principle of molecular divergence, followed by a second organizing principle, spatial separation, acting within respective neurogenesis groups to further differentiate temporally related IN subtypes. Thus, the final molecular identity of V3 IN subtypes requires the combination of both spatial and temporal neurogenesis parameters.

V3 IN spatial and temporal identities translate into functional distinctions

In addition to demonstrating that combined spatial and temporal factors organize V3 INs into distinct molecular clusters, our current study further illustrates that these factors bestow functional distinctions between V3 molecular subtypes. First, consistent with previous studies in zebrafish and mice[27,36,38], we found that subtype-specific neurogenesis timing determines post-mitotic V3 subtype axon projection profiles. Early-born V3 INs projected long axons while late-born V3 INs projected shorter axons projections. The latest born Prox1$^+$ V3 INs projected exclusively local commissural axons.

Furthermore, we demonstrated that temporal and spatial factors uniquely corresponded to the distinct morphological and electrophysiological properties of V3 molecular subtypes. Our data indicated that laminar settling position accounted for V3 electrophysiological diversification while neurogenesis timing accounted for V3 morphological diversification. Thus, early embryonic spatial and temporal factors likely serve as independent mechanisms combined across the V3 IN class to yield increasingly divergent subtypes. Several of the TFs that we identified here are also expressed in other spinal INs[12,15]. Thus, these temporal and spatial principles guiding V3 diversification may be shared by other spinal neurons.

Ultimately, we suggest that spatial and temporal settings may eventually account for V3's functional diversity across a wide repertoire of locomotor behaviours[19,23]. Using

post-activity c-fos expression as an activity indicator, our previous studies have shown that spatially separate dorsal and ventral V3 clusters – which could be denoted to Nr3b3$^+$ and Olig3$^+$ V3 INs, respectively – are recruited differently during different locomotor behaviors. For example, dorsal V3 INs, which have long ascending commissural projections, are activated during all overground activities, particularly at intermediate speeds or inclined running. In contrast, dorsal V3 INs displayed low recruitment levels during swimming[23]. These results may imply dorsal V3 IN involvement in the mediation of cutaneous sensory inputs. Furthermore, dorsal V3 INs may play more direct roles in the in the coordination of hindlimb-forelimb outputs necessary for overground locomotion. On the other hand, ventral V3 INs, which are directly involved in motor output[24] were active in all tested behaviors regardless of the specific locomotor task[23].

Here, we further examined the recruitment patterns of the two spatially overlapping but temporally separate Pou2f2$^+$ and Prox1$^+$ V3 INs. We found while Pou2f2$^+$ V3 INs displayed heightened c-fos expression following all sensorimotor tasks performed, Prox1$^+$ V3 INs selectively displayed c-fos expression following hindlimb loading and balance-dependent behaviours – not speed-dependent nor swimming locomotion. Thus, in addition to molecular and anatomical restriction, late-born Prox1$^+$ V3 INs were also functionally restricted to balance- and load-specific locomotors tasks.

These findings may indicate a fundamental principle for the formation of neuronal circuits; neuronal connections form when at the right place and the right time to meet their right partner. That is, the spatial and temporal control over when a V3 IN becomes post-mitotic may restrict its pre- and post-synaptic targets available. One such principal was eloquently demonstrated in zebrafish, where dI6 INs form inhibitory synaptic contacts on the motor neuron compartments available at the time they become postmitotic[38]. Early-born dI6 INs form synaptic connections onto motor neuron somas before motor neurons begin projecting neurites. Later-born dI6 INs then form synaptic connections onto motor neuron dendrites as motor neurons begin projecting neurites in alignment with late-born dI6 neurogenesis timing.

In the case of V3 IN subpopulations, the neurogenesis timing of early-born Prou2f2$^+$ V3 INs would be in parallel with the formation of surrounding spinal locomotor circuits and incoming sensory afferents. As a result, early born Pou2f2$^+$ V3 INs were wildly recruited across varied locomotor tasks. In contrast, when sensory afferents enter the mouse spinal cord at early embryonic timepoints[39], late-born Prox1$^+$ V3 INs are still exiting the p3 progenitor domain without neurite projections. Thus, Prox1$^+$ V3 INs may “miss” early incoming sensory afferents and solely receive later descending supraspinal inputs restricting their functional locomotor recruitments. Later born V3 INs may therefore layer more complex sensorimotor functional outputs on top of an underlying core locomotor circuit formed by early-born V3 INs

Taken together, our work here provides exciting new avenues towards understanding how early temporal and spatial mechanisms combine to construct IN subtype diversities, circuit connectivities and ultimately functional recruitments across diverse locomotor behaviours. We have uncovered the molecular, anatomical, and physiological subtype diversity of the

cardinal V3 IN class in the mammalian lumbar spinal cord. Furthermore, we have revealed the key developmental spatial and temporal logic underlying this V3 diversification. Our work lends to our growing understanding of how spinal INs differentiate into functionally distinct circuit modules from embryonic to postnatal stages.

Limitations of the Study

The biggest limitation of our work is that the TFs that we have tested here are mainly from the sequencing data of embryonic spinal cords. The expression of these TFs gradually decreases or changes postnatally. Therefore, our recordings were performed in the animals between P7-P10, when spinal INs (including V3s), were not fully mature and some of their intrinsic properties are still changing[29]. Accordingly, our characterization of each V3 IN subpopulation might not be fully complete. In addition, due to the weak expression of these markers our posthoc recovery of the recorded cells was very low, which made a true cluster analysis[40] impossible. We were additionally unable to reliably label Onecut2^{+} V3 INs via post-hoc patch-clamp biotin staining at postnatal ages due to the diminished staining. Despite these disadvantages, our work was able to delineate four molecularly distinct V3 IN subpopulations along a spatiotemporal axis revealing the developmental logic delineating their anatomical and functional separations.

STAR★Methods

RESOURCE AVAILABILITY

Lead contact—Further information and requests for resources and reagents should be directed to and will be fulfilled by the Lead Contact, Ying Zhang (Ying.Zhang@dal.ca)

Materials availability—This study did not generate new unique reagents.

Data and code availability

- **Data** reported in this paper will be shared by the lead contact upon request.
- This paper does not report original **code**.
- Any additional information required to reanalyze the data reported in this paper is available from the lead contact upon request.

Experimental model and study participant details

Mice: In all our experiments, we used male and female mice equally. The mouse strains and breeding strategies are indicated as following. Sim1^{Cre} mice[20] were crossed with TdTomato (TdTom) Ai14 conditional reporter mice (Jackson Laboratory) to generate Sim1^{Cre};Rosa.lsl.tdTom mice[20,22] used for fate mapping of Sim1^{+} V3 INs at embryonic and postnatal stages. To generate Sim1Cre;NestinFlpoER;Ai65D, we established a first generation cross between Sim1Cre male mice with NestinFlpoER[41,42] female mice. We then established a second generation cross between Sim1Cre;NestinFlpoER male mice and Ai65D female mice (Jackson Laboratory) containing tdTomato downstream of both a frt-flanked and a loxP-flanked STOP cassette. All procedures were performed in accordance

with the Canadian Council on Animal Care and approved by the University Committee on Laboratory Animals at Dalhousie University.

METHOD DETAILS

Spinal cord tissue dissection, processing and sectioning—Spinal cords were obtained at embryonic and postnatal stages. For embryonic staging, the date of fertilization was identified by the presence of a vaginal plug, and the morning of vaginal plug discovery was defined as E0.5. Prior to dissection of embryos, pregnant mothers were anaesthetized via intraperitoneal injections of a ketamine (60mg/kg) and xylazine (12mg/kg) cocktail. Once a mouse no longer responded to the pedal reflex, it was decapitated and embryos removed via cesarean section. Embryonic and postnatal mice were euthanized via decapitation and spinal cords subsequently dissected in Ringer's Solution (111mM NaCl, 3.08 mM KCl, 11mM glucose, 25 mM NaHCO3, 1.25 mM MgSO4, 2.52 mM CaCl2, 1.18 mM KH2PO4) bubbled with 95%O2/5%CO2 to maintain a pH of 7.4. Spinal cords were fixed with 4% paraformaldehyde (Electron Microscopy Sciences) [PFA] in phosphate-buffered saline (PBS) at 4°C for varying times (E9.5, 10 mins; E10.5 and E11.5, 15 mins; E12.5, 25 mins; E13.5, 30 mins; E14.5, 35 mins; P0, 1h). Spinal cords were then washed in PBS 3 times for 15 mins each and then overnight at 4°C. The following day, spinal cords were cryoprotected in 20% sucrose in PBS at 4°C overnight.

For postnatal tissue extraction, mice were anaesthetized via intraperitoneal injections of a ketamine (60mg/kg) and xylazine (12mg/kg) cocktail prior to perfusion. Once a mouse no longer responded to the pedal reflex, they were transcardially perfused with phosphate-buffered saline (PBS) and then 4% paraformaldehyde (Electron Microscopy Sciences) [PFA] in PBS. Following perfusion, spinal cords were dissected and incubated in 4% PFA for 1h (≤P7) or 4h (≥P21) on ice. Spinal cords were then washed in PBS three times for 20mins each on ice followed by overnight in PBS at 4°C. Subsequently spinal cords were cryoprotected in 30% sucrose in PBS at 4°C for 2–3 nights.

Tissues were embedded in O.C.T compound (Fisher Healthcare) and flash-frozen at −55°C in a dry ice/ethanol bath. Frozen lower thoracic and higher lumbar (T12-L3) cord segments were sectioned transversely using a cryostat (Leica CM1950). E9.5-E14.5 cords were sectioned at 14 micrometers and postnatal cords at 20 or 30 micrometers onto Superfrost Plus Microscope Slides (Fisherbrand).

Immunohistochemistry—Mounted sections were first incubated in PBS containing 0.1% Triton X (PBS-T) for 3 washes of 5–15 minutes each. Subsequently, sections were incubated in PBS containing primary antibodies and 10% heat-inactivated horse serum (Invitrogen) overnight at 4°C. Primary antibodies used are listed in Table 1. Following primary antibody incubation, sections were washed three times with PBS for 5–15 mins each then incubated in PBS containing secondary anti-bodies (and Alexa Fluor conjugated streptavidin when relevant) for 1h at 4°C. Secondary antibodies used are listed in Table 1. When applicable, secondary antibody incubation was followed by Click-iT® EdU Alexa Fluor® 647 fluorescent labeling (Thermofisher). Lastly, sections were washed three times in PBS for 5–15 mins each and cover-slipped with fluorescent mounting medium (Dako).

Image capture and laminar cell position analysis—Fluorescent micrographs of sections were captured using a Zeiss LSM 710 upright confocal microscope with ZEN 2009 Microscope and Imaging Software. Cell numbers and laminar positions were quantified using ImageJ and MATLAB. Using the ImageJ Cell Counter Plugin, x,y coordinates of individual cell bodies as well as the maximum and minimum x,y coordinates of corresponding spinal cord outlines were denoted. At postnatal stages (P0, ≥P21), a total of 10 randomly chosen 30 μm transverse sections were analyzed between and including T12 to L3 per animal. At embryonic time points (E10.5-E14.5) a total of 10 randomly chosen 14 μm transverse sections were analyzed within approximate lower thoracic and higher lumbar segments per animal. Cell body laminar distribution and cell body density contour plots were subsequently constructed utilizing *grid-data* and *contour* functions in MATLAB. Briefly, within each section, cell body x,y positions were normalized against maximum and minimum hemicord x,y coordinates. Cell density plots and Heat maps were then constructed to display cell body laminar distributions across mediolateral and dorsoventral axes. In select cases, heat maps were then constructed to display cell body densities across the mediolateral and dorsoventral axes.

Tamoxifen injections—To restrict TdTom expression to progressively later-born neurogenesis time, pregnant Sim1Cre;NestinFlpoER;Ai65D mice were injected with tamoxifen [20mg/1ml corn oil (Sigma-Aldridge, C8267), 100 μl per mouse] one time at either E10.5, E11.5, or E12.5. For embryonic staging, the date of fertilization was identified by the presence of a vaginal plug, and the morning of vaginal plug discovery was defined as E0.5. Embryos from tamoxifen injected mice were collected at E14.5.

5-Ethynyl-2´-deoxyuridine (EdU) pulse labeling of V3 IN neurogenesis profiles —EdU (Thermo Fisher Scientific) was dissolved in saline solution to 6mg EdU/1ml saline. Pregnant $Sim1^{Cre}$;Rosa.lsl.tdTom mice were injected Intraperitoneally with EdU solution based on body weight (50μl/10g) at gestational stages E10.5, E11.5, or E12.5. Comparable mice injected at E9.5 were pulsed with 12mg/ml EdU solution. For embryonic staging, the date of fertilization was identified by the presence of a vaginal plug, and the morning of vaginal plug discovery was defined as E0.5. EdU-pulsed spinal cords were collected at E14.5. Fluorescent labeling of DNA-incorporated EdU was detected using a Click-iT® EdU Alexa Fluor® 647 Imaging Kit (Thermofisher). To determine neurogenesis profiles of molecularly distinct V3 IN subsets, fluorescent labeling of EdU was performed following immunohistochemistry.

Retrograde Biotin-Dextran-Amine tract tracing—Axonal projection patterns of E11.5-E14.5 V3 INs were determined using retrograde Biotin-Dextran-Amine (BDA) tracing of isolated $Sim1^{Cre}$;Rosa.lsl.tdTom cords. Immediately following spinal cord dissection, 3000 MW, lysine fixable, BDA (Molecular Probes) was inserted into one half of the higher lumbar spinal cord. Insertion sites had a rostrocaudal spread of approximately 700–1000μm in each direction (data not shown). For dual tracing experiments, E14.5 $Sim1^{Cre}$;Rosa.lsl.tdTom cords were injected with both Dextran, Alexa Fluor™ 488 (3000 MW, Invitrogen, cat# D34682) and Dextran, Biotin (3000 MW, Invitrogen, cat# D7135)

at respective rostrocaudal and left-right locations. Injected cords were incubated overnight (16–20h) in Ringer's Solution bubbled with 95%O2/5%CO2 at 20°C.

Following incubation, embryonic postnatal cords were fixed in 4% paraformaldehyde (Electron Microscopy Sciences) [PFA] in PBS at 4°C for varying times (E9.5, 10 mins; E10.5 and E11.5, 15 mins; E12.5, 25 mins; E13.5, 30 mins; E14.5). Spinal cords were then washed in PBS 3 times for 15 mins each and then overnight at 4°C. Following washing spinal cords were either processed for either biotin detection and tissue clearing or tissue sectioning and immunohistochemistry.

For tissue sectioning and immunohistochemistry, cords were subjected to aforementioned tissue processing procedures. These procedures are also described in detail elsewhere[22,43,44]. Fluorescent labeling of BDA was performed in concert with immunohistochemical labeling of spinal cord sections. Either Alexa Fluor 405-conjugated streptavidin (Thermofisher), Alexa Fluor 488-conjugated streptavidin (Thermofisher), or Alexa Fluor 647-conjugated streptavidin (Thermofisher) was diluted 1:500 and added to secondary antibody solutions.

Retrograde Chloera Toxin Subunit B tract tracing—Cholera Toxin Subunit B (CTB) conjugated with Alexa Fluor 488 (0.5mg/1ml PBS) [Molecular Probes] was injected into the unilateral cervical (C)7 spinal cord in P14 Sim1Cre;Rosa.lsl.tdTom mice. 7 days after CTB injections, animals were euthanized and spinal cords dissected at P21.

Patch-clamp recordings and post-hoc immunohistochemistry—P6-P12 Sim1Cre;Rosa.lsl.tdTom mice were decapitated and their higher lumbar spinal cords (L1-L3) dissected in ice-cold oxygenated sucrose Ringer's solution (3.5 mM KCL, 25 mM NaHCO3, 1.2 mM KH2PO4, 1.3 mM MgSO4, 1.2 mM CaCl2, 10 mM glucose, 212.5 mM sucrose, 2 mM MgCl2 × 6H2O, pH 7.4). After removing the roots and meninges, L1-L3 regions of spinal cords were embedded into low-melting agarose (2-hydroxyethylagarose, Aldrich-Sigma, A4018) and sectioned at 300–350 μm on a vibratome (7000smz-2 Vibrotome, Campden Instruments Ltd.). Slices were incubated in an oxygenated regular Ringer's solution (111mM NaCl, 3.08 mM KCl, 11mM glucose, 25 mM NaHCO3, 1.25 mM MgSO4, 2.52 mM CaCl2, 1.18 mM KH2PO4, pH 7.4) at room temperature for >30min for recovery prior to recording.

Following a recovery period, slices were transferred to a recording chamber mounted on an Olympus BX51WI microscope and perfused constantly with oxygenated (95% O2 + 5% CO2 to produce a pH of 7.4) room temperature Ringer's solution. TdTomato fluorescence positive V3 neurons were visually identified with a 40x water immersion objective (N.A. = 0.8) with the aid of a DAGE-MTI IR-1000 CCD camera.

Conventional whole-cell patch clamp recordings were made in voltage- and current-clamp modes using a MultiClamp 700B amplifier (Molecular Devices Inc., Sunnyvale, CA, USA). Analog signals were filtered at 10kHz with the Digidata 1400A board (Molecular Devices) under control of pCLAMP10.3 (Molecular Devices). Patch-clamp recording pipettes with a resistance of 5–8 mΩ were filled with a solution containing 128 mM K-gluconate, 4 mM NaCl, 0.0001 mM CaCl2, 10 mM HEPES, 1 mM glucose, 5 mM Mg-ATP, 0.3 mM GTP-Li,

pH 7.4. Then 0.4 mg lucifer yellow dilithium salt (Sigma-Aldrich, L0259) and 1mg/ml neurobiotin (SP-1120 Vector Laboratories, Inc Burlingame, CA 94010) were added to the pipette solution prior to recording to aid in mapping the V3 neurons that were recorded.

To assure the same measuring conditions, all cells were held at −60mV with a tonic DC current. Cells that required more than 250pA of holding current to maintain these potentials or had action potential amplitude <60 mV were excluded from the analyzed data. Capacitance and series resistance were not compensated.

Data were obtained by Clampfit 10.3 (Molecular Devices) and analysed by Clampfit 10.3 and Spike2 5.0 (Cambridge Electronic Design) software packages. Input resistance and capacitance were evaluated by measurements from the cells' response to repetitive, small negative steps (−10mV, 100 ms). The resting membrane potential was calculated by taking the average voltage over 10 seconds Immediately after patching the cell membrane.

To obtain the frequency-current (F-I) plots, 1 s current pulses with increments of 5, 10, 20 or 40 pA were applied to the cell. The average spike frequency was determined by counting the number of spikes during the 1 s pulse. The spike frequencies were plotted against the injected currents. In our experiments, the spike frequency of some small cells very quickly reached a plateau stage with the series of depolarization. To avoid mis-fitting the saturation phase, the F-I curve was fitted by the equation y=a*x/(1+x/b): a represented the initial linear slope of F-I plot; b was the presuming maximum spike frequency. The spike frequency adaptation ratio (SFA) was calculated by the average of last three inter-spike intervals were divided by the average of first three inter-spike intervals at the step the average spike frequency of the cell was at 10Hz. We also measured the rheobase, the spike latency, the amplitude, the half width, and the threshold of the first spike generated by the smallest suprathreshold current.

The subthreshold properties of the cells were obtained by applying 1s current pulses to different hyperpolarization membrane potentials. The amplitude of sag voltage was defined as the difference between the peak of hyperpolarized membrane potential and the steady-state voltage.

V3 molecular identities were determined via post-hoc immunohistochemistry. Briefly, following recording, spinal cord slices were fixed in 4% PFA for 10mins at room temperature. They were then washed over night in PBS. The following day, they were incubated in 0.1% PBS-T three times for approximately 30 mins each at room temperature on a shaker. They were then incubated in PBS containing primary antibodies and 10% heat-inactivated horse serum (Invitrogen) for two nights at 4°C. Following primary antibody incubation, sections were washed three times with PBS for 15–30 mins at room temperature on a shaker. They were then incubated in PBS containing secondary anti-bodies and Alexa Fluor 488-conjugated streptavidin (Thermofisher) overnight at 4°C. Spinal sections finally washed three more times in PBS for 15–30 mins at room temperature and cover-slipped with fluorescent mounting medium (Dako).

Morphology Reconstruction and Analysis—Biotin-filled V3 INs were imaged with a 40x objective using a Zeiss LSM 710 upright confocal microscope and ZEN 2009 Microscope and Imaging Software. Both z-stack (30–60μm) and stitching functions (4–16 tiles) were required to capture the full ranges of neural processes. Three-dimensional neural morphologies were constructed from confocal images with the 'filament tracer' function on Imaris Software. Both automated and semi-automated filament tracing modes were used. Cell body volumes were constructed using the 'surfaces' function.

Following morphology tracing, images were saved as two-dimensional tiff files further subjected to Sholl Analysis (from image) using the Automated Sholl Plugin in Fiji (Supplemental Figure11). Briefly, concentric circles were constructed at 2μm increments spanning out from the neurons cell body. The total number of dendrites intersecting at each circle of a specific radius was then calculated allowing for a quantitative analysis of V3 dendritic properties. For our purposes, we quantified the total number of dendritic interceptions between set radius distances (total intercepts 0–100μm, total intercepts 100–200μm, total intercepts 200–300μm, total intercepts 300–400μm, total intercepts 400–500μm), the summation of all dendritic interceptions (sum intercepts), the mean number of dendritic interceptions (mean intercepts), the maximum number of dendritic interceptions (max intercepts), the radius at which the maximum number of dendritic interceptions occurred (max intercept radius), and the farthest radius that dendritic interceptions cross (ending radius).

Intrinsic Property Analysis—Recorded V3 INs were categorized as either Nr3b3$^+$, Pou2f2$^+$, Olig3$^+$, or Prox1$^+$ V3 INs via post-hoc immunoreactivity and assigned electrophysiological and morphological properties. We were unable to reliably identify Onecut2$^+$ V3 INs (due to diminished Onecut2 immunoreactivity after P5), and so, Onecut2$^+$ V3 INs were not included in our analysis.

To identify electrophysiological and morphological predictors with significant differences between their mean values across the four V3 molecular subtypes we performed single-factor ANOVAs and Tukey's multiple comparisons test. A predictor was deemed significant if at least one group mean was statistically different than the other three. A significant predictor did not necessarily provide a means to separate the four groups. However, it was anticipated that some combination of predictors would provide good separation as assessed by supervised cluster analysis.

Principal component analysis (PCA) was carried out to assess potential separation of the four groups using significant electrophysiological predictors alone, significant morphological predictors alone, and a combination of select electrophysiological and morphological predictors. PC1 and PC2 scores were plotted to visualize potential group separation. PC1 and PC2 score were also respectively plotted against dorsoventral cell body positions. Positions were defined as a ratio between the minimum ventral point (0) of the spinal slice and the maximum dorsal point (1) of the spinal slice.

To provide a more objective quantitative analysis, electrophysiological and morphological predictors were standardized and subjected to supervised classification analysis using the

Classification Learner Application in MATLAB. We utilized the support vector machine (SVM) learner as it consistently produced the best classification accuracy.

We used the SVM learner across three different data sets: 1) only electrophysiological predictors (six total: capacitance, sage slope, sage amplitude (120mV), rheobase, rheobase first spike latency, AP threshold (first spike)); 2) only morphological predictors (four total: total intercepts (0–100μm), max intercepts, mean intercepts, cell body volume); and 3) a combination of both electrophysiological and morphological predictors (capacitance, sage slope, sage amplitude (120mV), rheobase, rheobase first spike latency, AP threshold (first spike), total Intercepts (0–100μm), max intercepts, mean intercepts, cell body volume). Model results were reported as confusion matrices of V3 subset prediction accuracies and error rates.

Task-specific recruitment behaviours—Task-specific neuronal recruitments were evaluated via c-fos immunostaining. c-fos is an activity dependent and immediate expression gene that can be used as a molecular marker of preceding neuronal activation. c-fos expression peaks approximately 1-hour post-activation[45,46] and is a reliable indicator of spinal neuron activation induced by locomotor stepping[23,47,48].

For Prox1^{+} and Pou2f2^{+} V3 IN recruitments, P21-P35 Sim1^{Cre};Rosa.lsl.tdTom mice were subjected to six distinct behavioural tasks, respectively. Upon completion of a behavioural task, mice were given 1h of recovery before spinal cord dissection. During the 1h of recovery, mice were placed into an empty cage without food or external stimulation. For no task, mice were left in an empty cage for 1 hour followed by perfusion and tissue extraction. Minimal c-fos expression was detected following no task (Supplemental Figure 13A).

Slow speed locomotion was achieved by subjecting mice to constant treadmill locomotion at a speed of 15 cm/s for 1 hour continuously – at this speed mice perform predominately a walking gait[49,50]. Intermediate speed locomotion was achieved by subjecting mice to three treadmill locomotor bouts of 15 minutes at 40 cm/s with 5 minutes rest between each bout – at this speed mice perform predominately a trotting gait[49,50]. For incline locomotion, mice were subjected to treadmill locomotion at 15 cm/s for 1h with a treadmill inclined at an angle of +25 degrees. For “staggered stepping” locomotion, mice were subjected to treadmill locomotion at 15 cm/s for 1h on a treadmill continuously oscillating side-to-side at a speed of 7cm/s. For “lateral motion”, mice stood stationary on a treadmill as it continuously oscillated side-to-side at a speed of 7cm/s, with no forward movement, for 1h. For swimming locomotion, mice were placed in a pool containing distilled water maintained at a temperature ranging from 30–35 degrees Celsius for 1 hour.

Quantification and statistical analysis

Data presented as mean ± standard deviation. Statistical analysis was performed in Prism 7 (GraphPad Software, Inc), using one-way ANOVA and Tukey’s multiple comparisons test, or Mann-Withney-Wilcoxin test. *, p-value <0.05; **, p-value <0.01; ***, p-value <0.001.

Supplementary Material

Refer to Web version on PubMed Central for supplementary material.

Acknowledgements

The authors thank for the generous gifts of *Sim1Cre* mouse from Dr. Martyn Goulding, Salk Institute for Biological Studies, CA, USA, and of *NestinFlpoERT2* mouse from Dr. Alexandra Joyner, Memorial Sloan Kettering Cancer Center, New York, USA. The authors also thank Dr. Turgay Akay, Dalhousie University, Canada for his assistant in the behavior tests, and Drs Tuan Bui, Kimberly Dougherty and Simon Gosgnach for their constructive comments on the early version of the manuscript. The research was funded by the Canadian Health Institutes of Research (MOP-110950 and PJT-173547 to Y.Z. and the Natural Sciences and Engineering Research Council of Canada (RGPIN 04880 YZ).

References

1. Gosgnach S, Bikoff JB, Dougherty KJ, El Manira A, Lanuza GM, and Zhang Y (2017). Delineating the Diversity of Spinal Interneurons in Locomotor Circuits. J Neurosci 37, 10835–10841. 10.1523/JNEUROSCI.1829-17.2017. [PubMed: 29118212]
2. Goulding M (2009). Circuits controlling vertebrate locomotion: moving in a new direction. Nat Rev Neurosci 10, 507–518. 10.1038/nrn2608. [PubMed: 19543221]
3. Deska-Gauthier D, & Zhang Y (2019). The functional diversity of spinal interneurons and locomotor control. Current Opinion in Physiology 8, 99–108.
4. Jessell TM (2000). Neuronal specification in the spinal cord: inductive signals and transcriptional codes. Nat Rev Genet 1, 20–29. 10.1038/35049541. [PubMed: 11262869]
5. Arber S (2012). Motor circuits in action: specification, connectivity, and function. Neuron 74, 975–989. 10.1016/j.neuron.2012.05.011. [PubMed: 22726829]
6. Kiehn O (2016). Decoding the organization of spinal circuits that control locomotion. Nat Rev Neurosci 17, 224–238. 10.1038/nrn.2016.9. [PubMed: 26935168]
7. Lu DC, Niu T, and Alaynick WA (2015). Molecular and cellular development of spinal cord locomotor circuitry. Front Mol Neurosci 8, 25. 10.3389/fnmol.2015.00025. [PubMed: 26136656]
8. Russ DE, Cross RBP, Li L, Koch SC, Matson KJE, Yadav A, Alkaslasi MR, Lee DI, Le Pichon CE, Menon V, and Levine AJ (2021). A harmonized atlas of mouse spinal cord cell types and their spatial organization. Nat Commun 12, 5722. 10.1038/s41467-021-25125-1. [PubMed: 34588430]
9. Alkaslasi MR, Piccus ZE, Hareendran S, Silberberg H, Chen L, Zhang Y, Petros TJ, and Le Pichon CE (2021). Single nucleus RNA-sequencing defines unexpected diversity of cholinergic neuron types in the adult mouse spinal cord. Nat Commun 12, 2471. 10.1038/s41467-021-22691-2. [PubMed: 33931636]
10. Baek M, Menon V, Jessell TM, Hantman AW, and Dasen JS (2019). Molecular Logic of Spinocerebellar Tract Neuron Diversity and Connectivity. Cell Rep 27, 2620–2635 e2624. 10.1016/j.celrep.2019.04.113. [PubMed: 31141687]
11. Blum JA, Klemm S, Shadrach JL, Guttenplan KA, Nakayama L, Kathiria A, Hoang PT, Gautier O, Kaltschmidt JA, Greenleaf WJ, and Gitler AD (2021). Single-cell transcriptomic analysis of the adult mouse spinal cord reveals molecular diversity of autonomic and skeletal motor neurons. Nat Neurosci 24, 572–583. 10.1038/s41593-020-00795-0. [PubMed: 33589834]
12. Delile J, Rayon T, Melchionda M, Edwards A, Briscoe J, and Sagner A (2019). Single cell transcriptomics reveals spatial and temporal dynamics of gene expression in the developing mouse spinal cord. Development 146. 10.1242/dev.173807.
13. Haring M, Zeisel A, Hochgerner H, Rinwa P, Jakobsson JET, Lonnerberg P, La Manno G, Sharma N, Borgius L, Kiehn O, et al. (2018). Neuronal atlas of the dorsal horn defines its architecture and links sensory input to transcriptional cell types. Nat Neurosci 21, 869–880. 10.1038/s41593-018-0141-1. [PubMed: 29686262]
14. Hayashi M, Hinckley CA, Driscoll SP, Moore NJ, Levine AJ, Hilde KL, Sharma K, and Pfaff SL (2018). Graded Arrays of Spinal and Supraspinal V2a Interneuron Subtypes Underlie Forelimb

and Hindlimb Motor Control. Neuron 97, 869–884 e865. 10.1016/j.neuron.2018.01.023. [PubMed: 29398364]

15. Osseward PJ 2nd, Amin ND, Moore JD, Temple BA, Barriga BK, Bachmann LC, Beltran F Jr., Gullo M, Clark RC, Driscoll SP, et al. (2021). Conserved genetic signatures parcellate cardinal spinal neuron classes into local and projection subsets. Science 372, 385–393. 10.1126/science.abe0690. [PubMed: 33888637]
16. Rosenberg AB, Roco CM, Muscat RA, Kuchina A, Sample P, Yao Z, Graybuck LT, Peeler DJ, Mukherjee S, Chen W, et al. (2018). Single-cell profiling of the developing mouse brain and spinal cord with split-pool barcoding. Science 360, 176–182. 10.1126/science.aam8999. [PubMed: 29545511]
17. Sathyamurthy A, Johnson KR, Matson KJE, Dobrott CI, Li L, Ryba AR, Bergman TB, Kelly MC, Kelley MW, and Levine AJ (2018). Massively Parallel Single Nucleus Transcriptional Profiling Defines Spinal Cord Neurons and Their Activity during Behavior. Cell Rep 22, 2216–2225. 10.1016/j.celrep.2018.02.003. [PubMed: 29466745]
18. Danner SM, Zhang H, Shevtsova NA, Borowska-Fielding J, Deska-Gauthier D, Rybak IA, and Zhang Y (2019). Spinal V3 Interneurons and Left-Right Coordination in Mammalian Locomotion. Front Cell Neurosci 13, 516. 10.3389/fncel.2019.00516. [PubMed: 31824266]
19. Zhang H, Shevtsova NA, Deska-Gauthier D, Mackay C, Dougherty KJ, Danner SM, Zhang Y, and Rybak IA (2022). The role of V3 neurons in speed-dependent interlimb coordination during locomotion in mice. Elife 11. 10.7554/eLife.73424.
20. Zhang Y, Narayan S, Geiman E, Lanuza GM, Velasquez T, Shanks B, Akay T, Dyck J, Pearson K, Gosgnach S, et al. (2008). V3 spinal neurons establish a robust and balanced locomotor rhythm during walking. Neuron 60, 84–96. 10.1016/j.neuron.2008.09.027. [PubMed: 18940590]
21. Lin S, Li Y, Lucas-Osma AM, Hari K, Stephens MJ, Singla R, Heckman CJ, Zhang Y, Fouad K, Fenrich KK, and Bennett DJ (2019). Locomotor-related V3 interneurons initiate and coordinate muscles spasms after spinal cord injury. J Neurophysiol 121, 1352–1367. 10.1152/jn.00776.2018. [PubMed: 30625014]
22. Blacklaws J, Deska-Gauthier D, Jones CT, Petracca YL, Liu M, Zhang H, Fawcett JP, Glover JC, Lanuza GM, and Zhang Y (2015). Sim1 is required for the migration and axonal projections of V3 interneurons in the developing mouse spinal cord. Dev Neurobiol 75, 1003–1017. 10.1002/dneu.22266. [PubMed: 25652362]
23. Borowska J, Jones CT, Zhang H, Blacklaws J, Goulding M, and Zhang Y (2013). Functional subpopulations of V3 interneurons in the mature mouse spinal cord. J Neurosci 33, 18553–18565. 10.1523/JNEUROSCI.2005-13.2013. [PubMed: 24259577]
24. Chopek JW, Nascimento F, Beato M, Brownstone RM, and Zhang Y (2018). Sub-populations of Spinal V3 Interneurons Form Focal Modules of Layered Pre-motor Microcircuits. Cell Rep 25, 146–156 e143. 10.1016/j.celrep.2018.08.095. [PubMed: 30282024]
25. Bikoff JB, Gabitto MI, Rivard AF, Drobac E, Machado TA, Miri A, Brenner-Morton S, Famojure E, Diaz C, Alvarez FJ, et al. (2016). Spinal Inhibitory Interneuron Diversity Delineates Variant Motor Microcircuits. Cell 165, 207–219. 10.1016/j.cell.2016.01.027. [PubMed: 26949184]
26. Francius C, Harris A, Rucchin V, Hendricks TJ, Stam FJ, Barber M, Kurek D, Grosveld FG, Pierani A, Goulding M, and Clotman F (2013). Identification of multiple subsets of ventral interneurons and differential distribution along the rostrocaudal axis of the developing spinal cord. PLoS One 8, e70325. 10.1371/journal.pone.0070325. [PubMed: 23967072]
27. Satou C, Kimura Y, and Higashijima S (2012). Generation of multiple classes of V0 neurons in zebrafish spinal cord: progenitor heterogeneity and temporal control of neuronal diversity. J Neurosci 32, 1771–1783. 10.1523/JNEUROSCI.5500-11.2012. [PubMed: 22302816]
28. Ruder L, Takeoka A, and Arber S (2016). Long-Distance Descending Spinal Neurons Ensure Quadrupedal Locomotor Stability. Neuron 92, 1063–1078. 10.1016/j.neuron.2016.10.032. [PubMed: 27866798]
29. Borowska J, Jones CT, Deska-Gauthier D, and Zhang Y (2015). V3 interneuron subpopulations in the mouse spinal cord undergo distinctive postnatal maturation processes. Neuroscience 295, 221–228. 10.1016/j.neuroscience.2015.03.024. [PubMed: 25800308]

30. Osseward PJ 2nd, and Pfaff SL (2019). Cell type and circuit modules in the spinal cord. Curr Opin Neurobiol 56, 175–184. 10.1016/j.conb.2019.03.003. [PubMed: 30954861]

31. Zeng H (2022). What is a cell type and how to define it? Cell 185, 2739–2755. 10.1016/j.cell.2022.06.031. [PubMed: 35868277]

32. Ampatzis K, Song J, Ausborn J, and El Manira A (2014). Separate microcircuit modules of distinct v2a interneurons and motoneurons control the speed of locomotion. Neuron 83, 934–943. 10.1016/j.neuron.2014.07.018. [PubMed: 25123308]

33. Deska-Gauthier D, and Zhang Y (2021). The Temporal Mechanisms Guiding Interneuron Differentiation in the Spinal Cord. Int J Mol Sci 22. 10.3390/ijms22158025.

34. Benito-Gonzalez A, and Alvarez FJ (2012). Renshaw cells and Ia inhibitory interneurons are generated at different times from p1 progenitors and differentiate shortly after exiting the cell cycle. J Neurosci 32, 1156–1170. 10.1523/JNEUROSCI.3630-12.2012. [PubMed: 22279202]

35. Stam FJ, Hendricks TJ, Zhang J, Geiman EJ, Francius C, Labosky PA, Clotman F, and Goulding M (2012). Renshaw cell interneuron specialization is controlled by a temporally restricted transcription factor program. Development 139, 179–190. 10.1242/dev.071134. [PubMed: 22115757]

36. Deska-Gauthier D, Borowska-Fielding J, Jones CT, and Zhang Y (2020). The Temporal Neurogenesis Patterning of Spinal p3-V3 Interneurons into Divergent Subpopulation Assemblies. J Neurosci 40, 1440–1452. 10.1523/JNEUROSCI.1518-19.2019. [PubMed: 31826942]

37. Sagner A, Zhang I, Watson T, Lazaro J, Melchionda M, and Briscoe J (2021). A shared transcriptional code orchestrates temporal patterning of the central nervous system. PLoS Biol 19, e3001450. 10.1371/journal.pbio.3001450. [PubMed: 34767545]

38. Kishore S, Cadoff EB, Agha MA, and McLean DL (2020). Orderly compartmental mapping of premotor inhibition in the developing zebrafish spinal cord. Science 370, 431–436. 10.1126/science.abb4608. [PubMed: 33093104]

39. Shepherd IT, Luo Y, Lefcort F, Reichardt LF, and Raper JA (1997). A sensory axon repellent secreted from ventral spinal cord explants is neutralized by antibodies raised against collapsin-1. Development 124, 1377–1385. 10.1242/dev.124.7.1377. [PubMed: 9118808]

40. Garcia-Ramirez DL, Singh S, McGrath JR, Ha NT, and Dougherty KJ (2022). Identification of adult spinal Shox2 neuronal subpopulations based on unbiased computational clustering of electrophysiological properties. Front Neural Circuits 16, 957084. 10.3389/fncir.2022.957084. [PubMed: 35991345]

41. Lao Z, Raju GP, Bai CB, and Joyner AL (2012). MASTR: a technique for mosaic mutant analysis with spatial and temporal control of recombination using conditional floxed alleles in mice. Cell Rep 2, 386–396. 10.1016/j.celrep.2012.07.004. [PubMed: 22884371]

42. Wojcinski A, Lawton AK, Bayin NS, Lao Z, Stephen DN, and Joyner AL (2017). Cerebellar granule cell replenishment postinjury by adaptive reprogramming of Nestin(+) progenitors. Nat Neurosci 20, 1361–1370. 10.1038/nn.4621. [PubMed: 28805814]

43. Eide AL, and Glover JC (1995). Development of the longitudinal projection patterns of lumbar primary sensory afferents in the chicken embryo. J Comp Neurol 353, 247–259. 10.1002/cne.903530207. [PubMed: 7745134]

44. Nissen UV, Mochida H, and Glover JC (2005). Development of projection-specific interneurons and projection neurons in the embryonic mouse and rat spinal cord. J Comp Neurol 483, 30–47. 10.1002/cne.20435. [PubMed: 15672401]

45. Barros VN, Mundim M, Galindo LT, Bittencourt S, Porcionatto M, and Mello LE (2015). The pattern of c-Fos expression and its refractory period in the brain of rats and monkeys. Front Cell Neurosci 9, 72. 10.3389/fncel.2015.00072. [PubMed: 25814929]

46. Muller R, Bravo R, Burckhardt J, and Curran T (1984). Induction of c-fos gene and protein by growth factors precedes activation of c-myc. Nature 312, 716–720. 10.1038/312716a0. [PubMed: 6334806]

47. Ahn SN, Guu JJ, Tobin AJ, Edgerton VR, and Tillakaratne NJ (2006). Use of c-fos to identify activity-dependent spinal neurons after stepping in intact adult rats. Spinal Cord 44, 547–559. 10.1038/sj.sc.3101862. [PubMed: 16344852]

48. Merkulyeva N, Veshchitskii A, Gorsky O, Pavlova N, Zelenin PV, Gerasimenko Y, Deliagina TG, and Musienko P (2018). Distribution of Spinal Neuronal Networks Controlling Forward and Backward Locomotion. J Neurosci 38, 4695–4707. 10.1523/JNEUROSCI.2951-17.2018. [PubMed: 29678875]

49. Bellardita C, and Kiehn O (2015). Phenotypic characterization of speed-associated gait changes in mice reveals modular organization of locomotor networks. Curr Biol 25, 1426–1436. 10.1016/j.cub.2015.04.005. [PubMed: 25959968]

50. Lemieux M, Josset N, Roussel M, Couraud S, and Bretzner F (2016). Speed-Dependent Modulation of the Locomotor Behavior in Adult Mice Reveals Attractor and Transitional Gaits. Front Neurosci 10, 42. 10.3389/fnins.2016.00042. [PubMed: 26941592]

51. Laumonnerie C, Tong YG, Alstermark H, and Wilson SI (2015). Commissural axonal corridors instruct neuronal migration in the mouse spinal cord. Nat Commun 6, 7028. 10.1038/ncomms8028. [PubMed: 25960414]

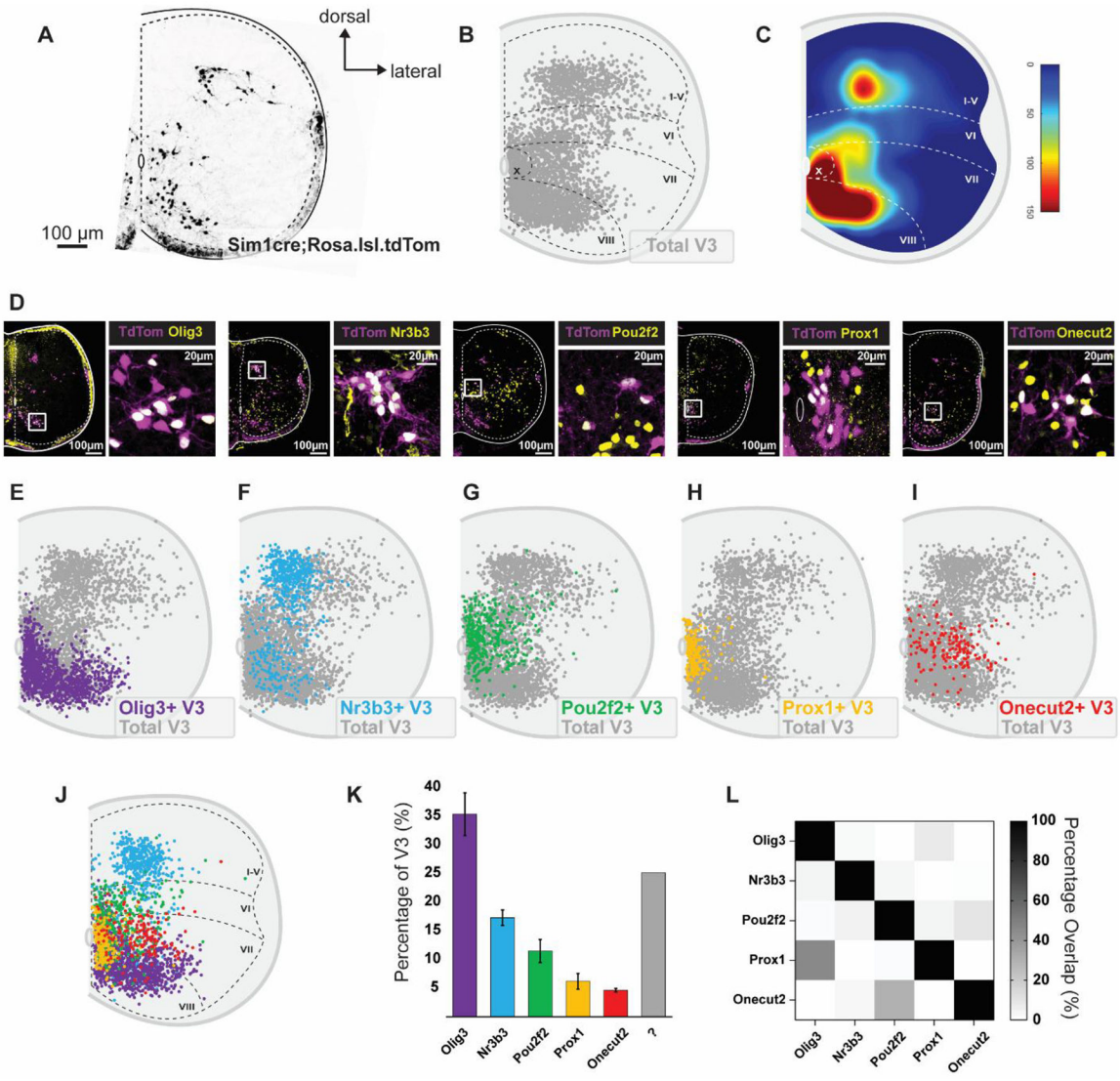

Figure 1. Molecularly subdivided V3 INs assemble into distinct topographical clusters.

(A) Representative image of TdTom^{+} V3 INs in an L2 spinal cord section from a Sim1^{Cre};Rosa.lsl.tdTom P0 mouse. (B-C) TdTom^{+} V3 laminar distribution plot (B) and density heat map plot (C) of the higher lumbar spinal cord (L1-L3) at P0 (n=4 animals). (D) Immunohistochemical labeling of Olig3^{+}, Nr3b3^{+}, Pou2f2^{+}, Prox1^{+}, and Onecut2^{+} V3 IN (TdTom) subsets in rostral lumbar (L1-L3) segments at P0. (E-I) Laminar cell distribution plots of Olig3^{+} (E), Nr3b3^{+} (F), Pou2f2^{+} (G), Prox1^{+} (H), and Onecut2^{+} (I) V3 IN subsets in rostral lumbar (L1-L3) segments at P0 (n=4 animals for each V3 subset). (J) Combined laminar cell distribution plot of V3 IN subsets across rostral lumbar (L1-L3) segments at P0 (n=4 animals for each V3 subset). (K) Percentage of total V3 INs that express Olig3, Nr3b3, Pou2f2, Prox1, and Onecut2 in higher lumbar (L1-L3) segments at P0 (n=4 animals, error bars = standard deviation)(L) Matrix of pairwise transcription factor expression overlaps within single V3 INs.

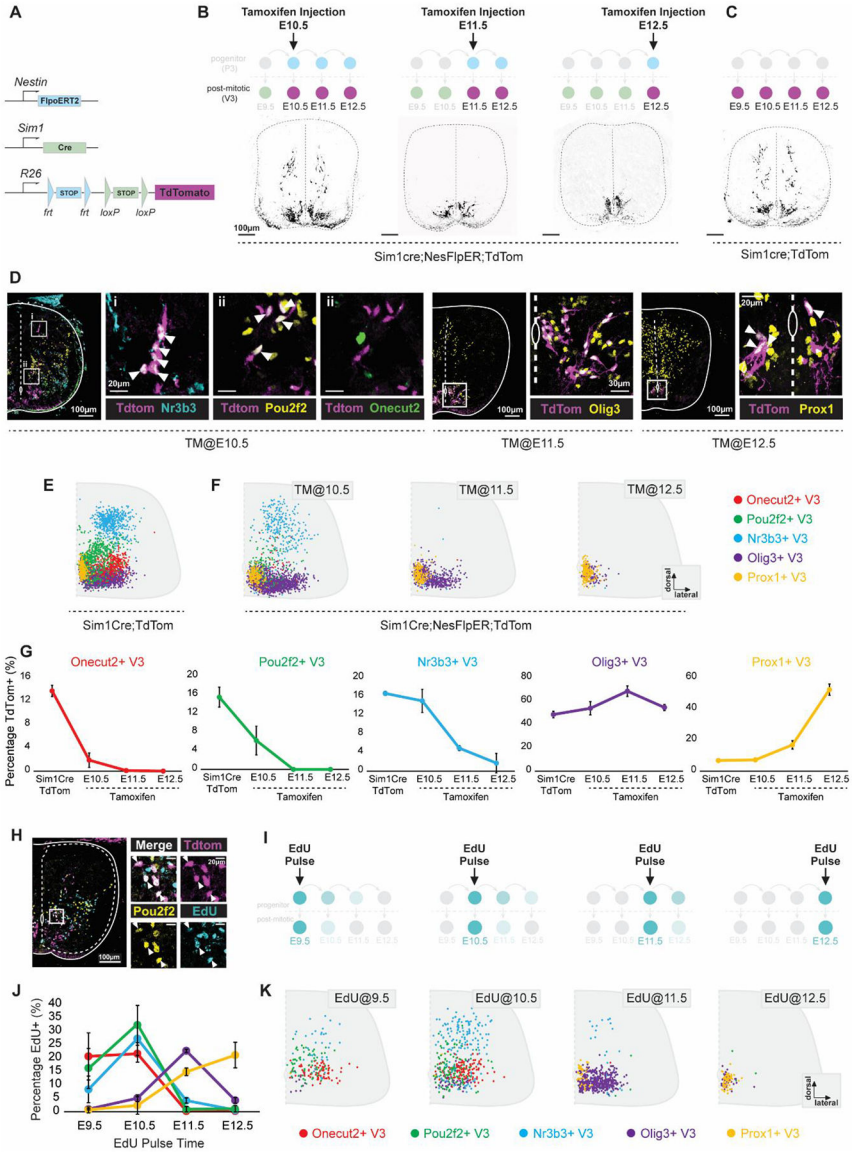

Figure 2. Molecularly and spatially distinct V3 IN subtypes emerge during early- or late-born neurogenesis windows.

(A) Sim1Cre;NestinFlpoER mice were crossed with Ai65D mice (Jackson Laboratory) containing tdTomato downstream of both a frt-flanked and loxP-flanked STOP cassette. Nestin is expressed in all dividing progenitor cells and Sim1 is expressed selectively in post-mitotic V3 INs. To restrict TdTom expression to later-born V3 INs, Flpo activation was induced via Tamoxifen injections at respective time points between E10.5-E12.5 in Sim1Cre;NestinFlpoER;Ai65D mice. (B) Experimental schematics and representative images of TdTom^{+} V3 INs from rostral lumbar slices at E14.5 in a Sim1Cre;NestinFlpoER;Ai65D mouse. Temporally restricted TdTom^{+} V3 INs were visualized at E14.5 following tamoxifen injections at either E10.5, E11.5, or E12.5. (C) Total V3 INs visualized in the rostral lumbar (L1-L3) spinal cord at E14.5 using a Sim1Cre;Rosa.lsl.tdTom mouse. (D) Post-hoc immunodetection of V3 molecular subsets at E14.5 of the higher lumbar spinal cord from Sim1Cre;NestinFlpoER;Ai65D mice injected

with tamoxifen at E10.5, E11.5, or E12.5. (E-F) Combined laminar cell distribution plot of V3 IN subsets in rostral lumbar (L1-L3) spinal segments at E14.5 from Sim1Cre;Rosa.lsl.tdTom mice (E), and Sim1Cre;NestinFlpoER;Ai65D mice injected with tamoxifen at E10.5, E11.5, or E12.5 (F). (G) Percentage of total $TdTom^+$ V3 INs that express Onecut2, Pou2f2, Nr3b3, Olig3, and Prox1 in Sim1Cre;Rosa.lsl.tdTom mice and Sim1Cre;NestinFlpoER;Ai65D mice injected with tamoxifen at E10.5, E11.5, or E12.5 (n=3 animals for each V3 subset and tamoxifen injection time, error bars = standard deviation). (H) Representative image of EdU detection in $Pou2f2^+$ V3 INs at E14.5 following an EdU pulse at E10.5 in a Sim1Cre;Rosa.lsl.tdTom mouse. (I) Experimental schematics EdU neurogenesis labeling between E9.5-E12.5. (J) Percentage of EdU^+ INs in V3 molecular subsets at E14.5 following EdU pulsing at E9.5, E10.5, E11.5, or E12.5 (n=3 animals for each V3 subset and EdU pulse time, error bars = standard deviation). (K) Combined laminar distribution plots of EdU^+ V3 molecular subsets at E14.5 in the rostral lumbar spinal cord (L1-L3) following EdU pulsing at E9.5, E10.5, E11.5, or E12.5 [n=3 animals for each V3 subset and EdU pulse time].

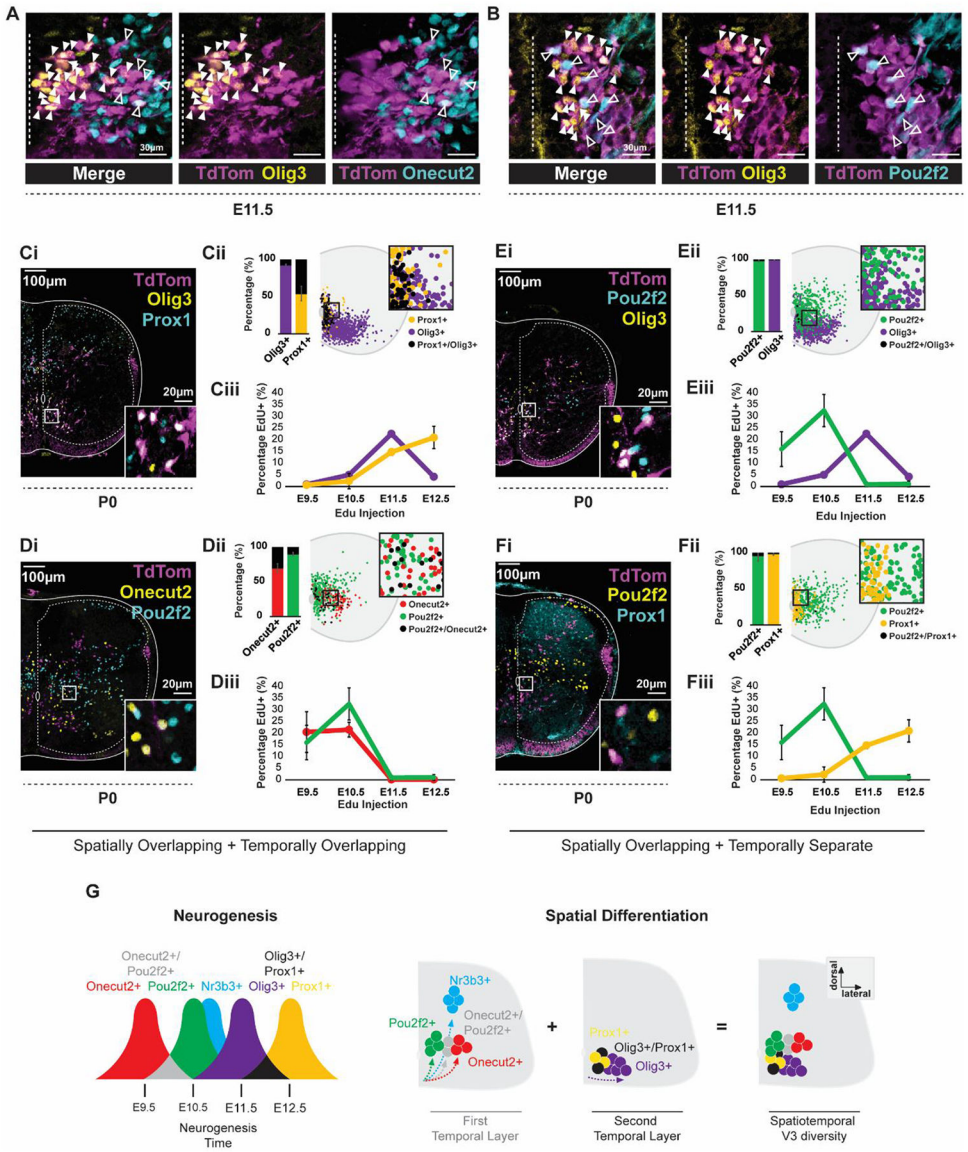

Figure 3. Combining laminar clustering with neurogenesis timing is necessary to differentiate V3 INs into molecularly distinct subpopulations.

(A-B) Representative images of Olig3 with Onecut2 (A) or Pou2f2 (B) immunoreactivity in V3 INs (TdTom$^+$) at E11.5 in *Sim1Cre;Rosa.lsl.tdTom* lumbar sections. (Ci-Fi) Representative images of dual transcription factor immunoreactivities in V3 INs (TdTom$^+$) in rostral lumbar (L1-L3) spinal cord sections from *Sim1Cre;Rosa.lsl.tdTom* P0 mice (Ci, Olig3-Prox1; Di, Onecut2-Pou2f2; Ei, Pou2f2-Olig2; Fi, Pou2f2-Prox1). (Cii-Fii) V3 laminar distribution plots of single expression and co-expression V3 INs (Cii, Olig3-Prox1; Dii, Onecut2-Pou2f2; Eii, Pou2f2-Olig2; Fii, Pou2f2-Prox1; n=4 animals per combination). (Ciii-Fiii) Neurogenesis profiles of V3 IN subsets expressing corresponding transcription factors at E14.5 (Ciii, Olig3& Prox1; Diii, Onecut2 & Pou2f2; Eiii, Pou2f2 & Olig2; Fiii, Pou2f2 & Prox1; n=3 animals for each V3 subset and EdU pulse time, error bars = standard deviation). (G) V3 molecular diversity emerges during embryogenesis through a combination of neurogenesis timing and post-mitotic spatial differentiation.

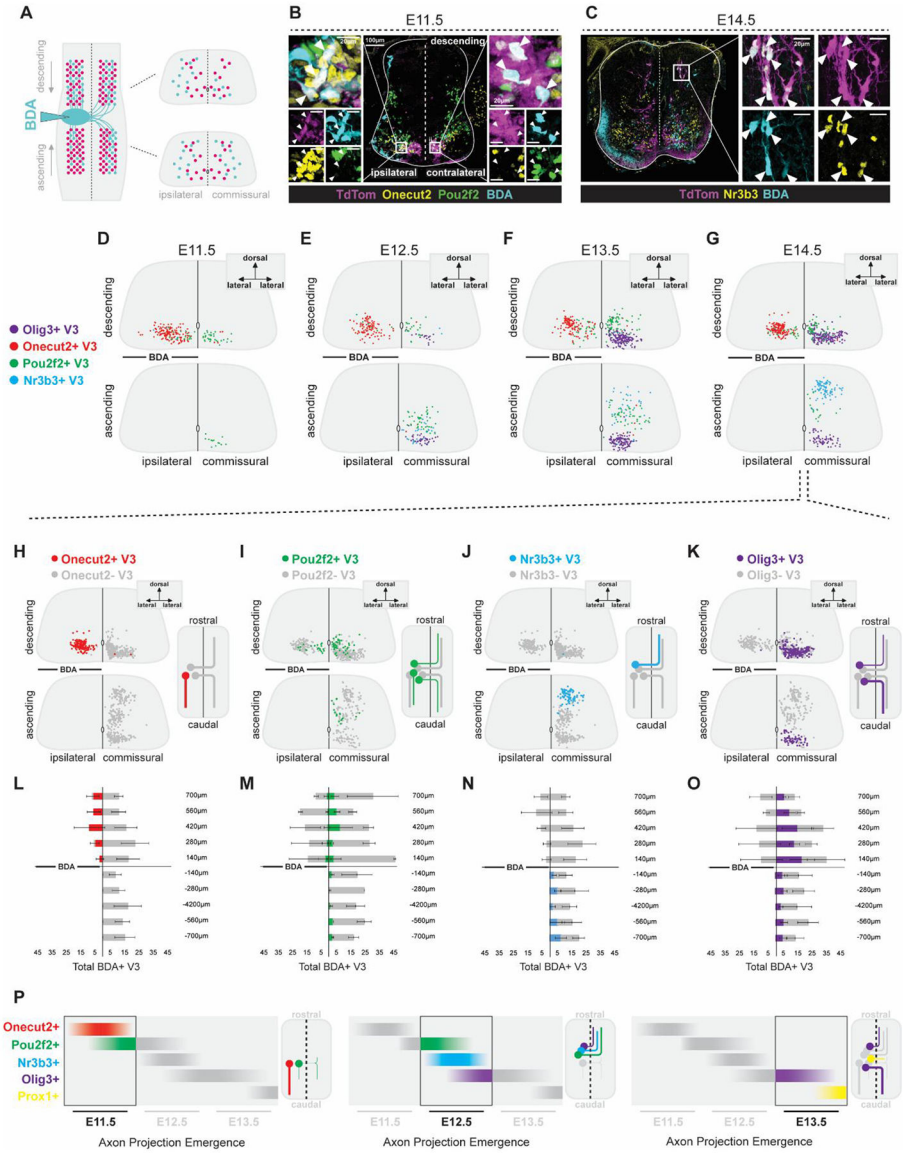

Figure 4. Post-mitotic V3 axon projection profiles emerge in a temporal order between E11.5-E14.5

(A) Experimental approach using retrograde biotin-dextran-amine (BDA) tracing in *Sim1Cre;Rosa.lsl.tdTom* mice to capture V3 axon projection profiles from E11.5-E14.5. (B-C) Representative images of cross sections from *Sim1^{Cre};Rosa.lsl.tdTom* spinal cords injected with BDA and immunostained post-hoc for V3 specific TFs at E11.5 (B) and E14.5 (C). (D-G) Cell distribution plots of Onecut2^{+}/BDA^{+}, Pou2f2^{+}/BDA^{+}, Nr3b3^{+}/BDA^{+}, and Olig3^{+}/BDA^{+} V3 INs rostral (descending), caudal (ascending), ipsilateral, and contralateral to the BDA injection site at E11.5 (D, n=3 animals for each V3 IN subset), E12.5 (E, n=3 animals for each V3 IN subset), E13.5 (F, n=3 animals for each V3 IN subset), and E14.5 (G, n=3 animals for each V3 IN subset). (H-K) Cell distribution plots at E14.5 of BDA labelling of Onecut2^{+} (H), Pou2f2^{+} (I), Nr3b3^{+} (J) and Olig3^{+} (K) V3 INs rostral (descending), caudal (ascending), ipsilateral, and contralateral to the BDA injection site at E14.5 (n=3 animals for each V3 IN subset). (L-O) Total BDA^{+} and Onecut2^{+} (L), Pou2f2^{+}

(M), Nr3b3^{+} (N) and Olig3^{+} (O) V3 INs (n=3 animals for each V3 IN subset, error bars = standard deviation). (P) Schematic representation of Onecut2^{+}, Pou2f2^{+}, Nr3b3^{+}, Olig3^{+}, and Prox1^{+} V3 IN projection pattern emergences across embryonic development. As V3 molecular subtypes exit the p3 progenitor domain, their axons projections emerge in a temporal and spatial order between E11.5 to E13.5.

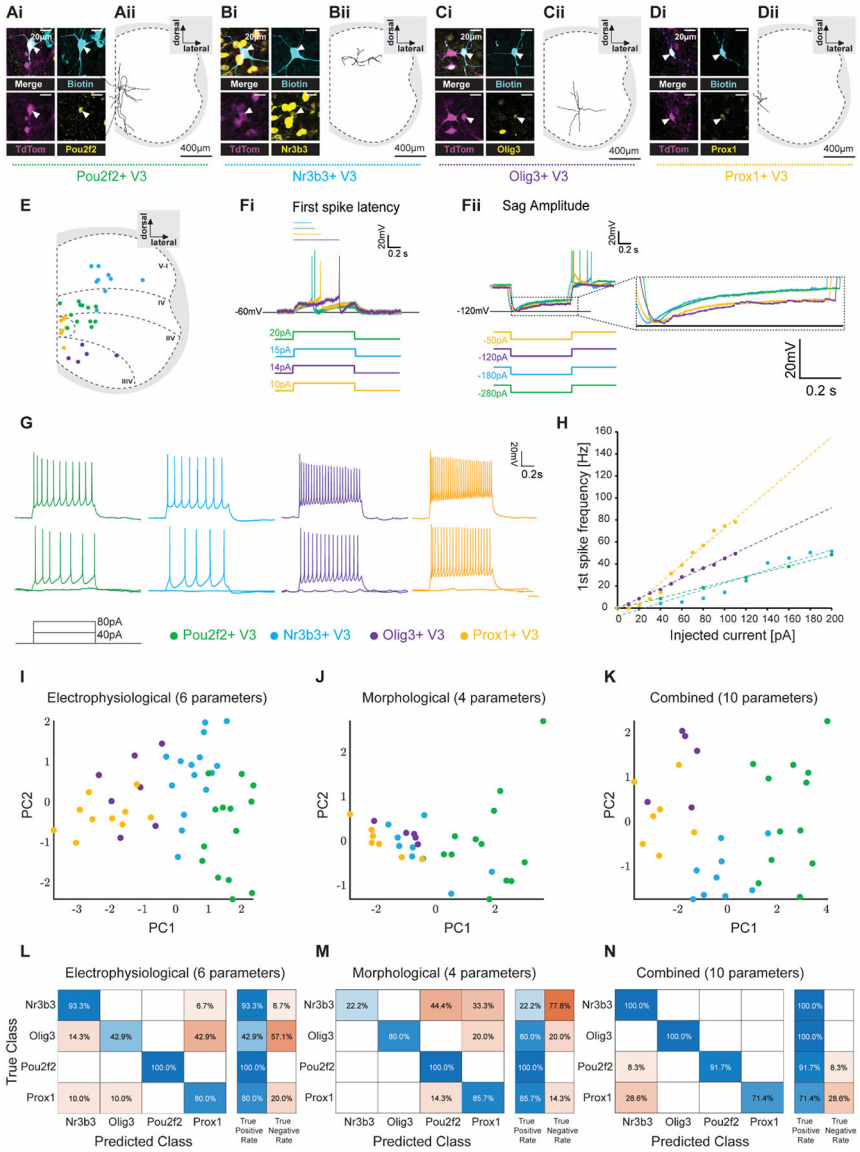

Figure 5. Combined electrophysiological and morphological properties separate V3 IN molecular subtypes into discrete clusters

(A-D) Post-hoc representative images of patch-clamped and biotin-filled V3 INs immunoreactive for Pou2f2^{+} (Ai), Nr3b3^{+} (Bi), Olig3^{+} (Ci), and Prox1^{+} (Di) between P7 and P12 of *Sim1^{Cre};Rosa.lsl.tdTom* rostral lumbar (L1-L3) spinal cord slices. Example morphology reconstructions of Nr3b3^{+} Pou2f2^{+} (Aii), Nr3b3^{+} (Bii), Olig3^{+} (Cii), and Prox1^{+} (Dii) V3 INs. (E) Laminar distributions of recorded Pou2f2^{+}, Nr3b3^{+}, Olig3^{+}, and Prox1^{+} V3 INs. (F) Representative current-clamp traces of Pou2f2^{+}, Nr3b3^{+}, Olig3^{+}, and Prox1^{+} V3 INs responding to 1s depolarizing (Fi) and hyperpolarizing (Fii) current injections. (G) Action potential firing patterns to 1s depolarizing current injections of 40pA (bottom) and 80pA (top). (H) Plot of first spike frequencies with increasing current injections. First (PC1) and second (PC2) principal component plots from electrophysiological (I), morphological (J), and combined (electrophysiological + morphological, K) principal component analyses of V3 molecular subtypes. V3 molecular

subtype prediction accuracies from a support vector machine (SVM) learner presented as confusion matrices of electrophysiological (L), morphological (M), and combined (electrophysiological + morphological, N) predictors.

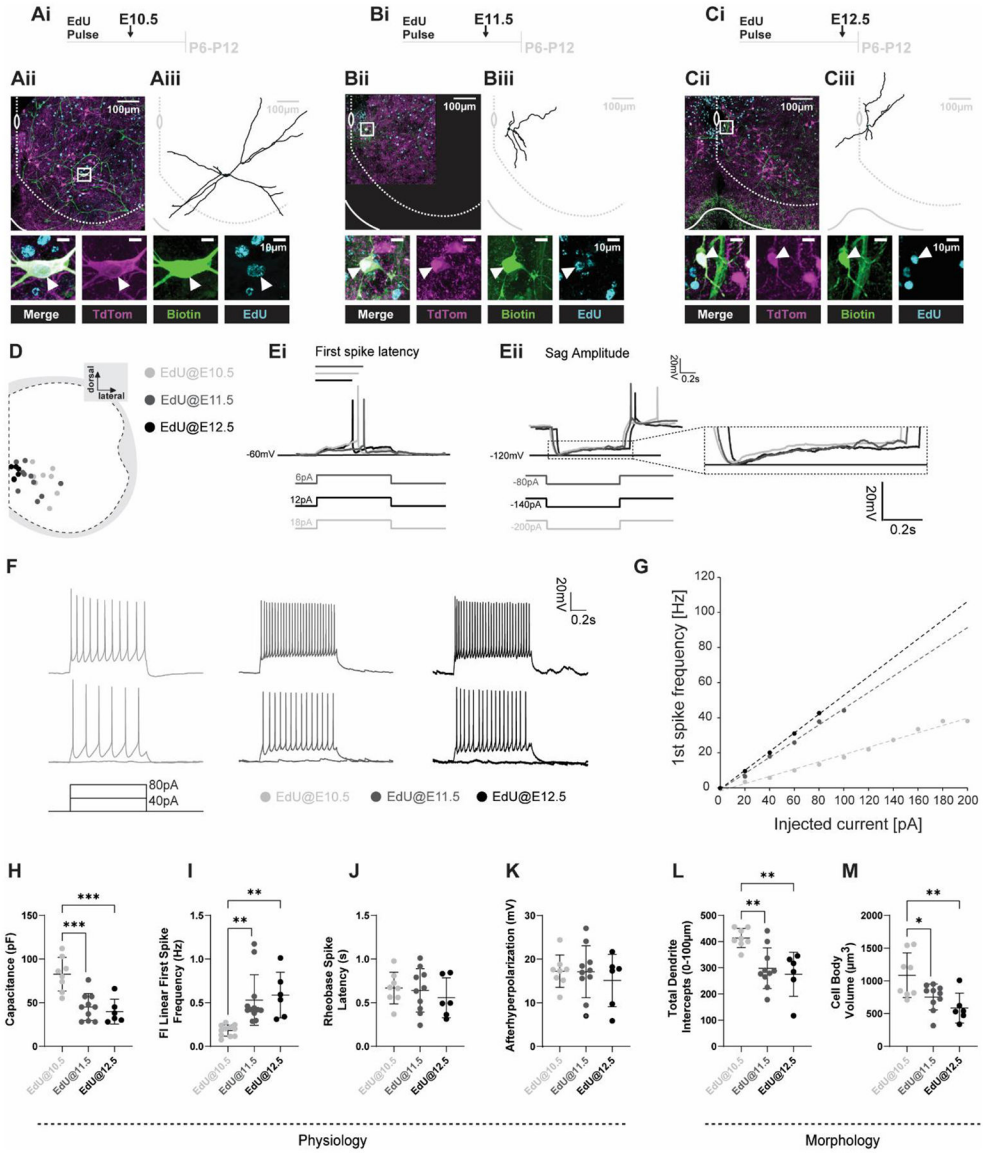

Figure 6. Neurogenesis timing separates V3 IN morphologies into early-born or late-born identities

(A-C) Experimental schematics of EdU injection and postnatal recording times (Ai, EdU@E10.5; Bi, EdU@11.5; Ci, EdU@E12.5). Representative images of patch-clamped and biotin-filled V3 INs immunoreactive for E10.5 EdU^{+} V3 (Aii), E11.5 EdU^{+} V3 (Bii), and E12.5 EdU^{+} V3 (Cii) between P6 and P12 in Sim1^{Cre};Rosa.lsl.tdTom rostral lumbar (L1-L3) spinal cord slices. Example morphology reconstructions of E10.5 EdU^{+} V3 (Aiii), E11.5 EdU^{+} V3 (Biii), and E12.5 EdU^{+} V3 INs (Ciii). (D) Laminar distributions of recorded E10.5 EdU^{+}, E11.5 EdU^{+}, and E12.5 EdU^{+} V3 INs. (E) Representative current-clamp traces of E10.5 EdU^{+}, E11.5 EdU^{+}, and E12.5 EdU^{+} V3 INs responding to 1s depolarizing (Ei) and hyperpolarizing (Eii) current injections. (F) Action potential firing patterns to 1s depolarizing current injections of 40pA (bottom) and 80pA (top). (G) Plot of first spike frequencies with increasing current injections. (H-K) Select electrophysiological parameters compared between neurogenically distinct V3 subsets (H, capacitance; I, F-I

linear first spike frequency; J, rheobase spike latency; K, afterhyperpolarization). (L-M) Select morphological parameters compared between neurogenically distinct V3 subsets (L, total dendritic intercepts (0–100μm); M, cell body volume) [*, p-value <0.05; **, p-value <0.01; ***, p-value <0.001; one-way ANOVA and Tukey's multiple comparisons test, error bars = standard deviation].

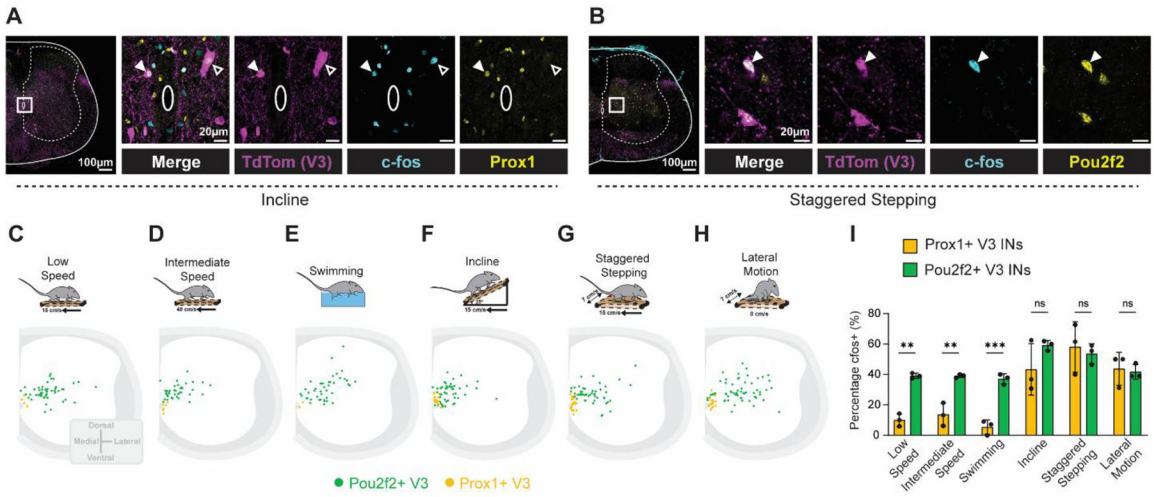

Figure 7. Prox1^{+} and Pou2f2^{+} V3 interneuron subpopulations display distinct sensorimotor recruitment patterns

(A-B) Representative images of c-fos^{+} immunoreactivities in Prox1^{+} V3 INs following incline locomotion (A) and Pou2f2^{+} V3 INs following staggered stepping (B) from rostral lumbar (L1-L3) spinal cord sections of adult Sim1Cre;Rosa.lsl.tdTom mice. Laminar cell distribution plots of c-fos^{+}/Pou2f2^{+} and c-fos^{+}/Prox1^{+} V3 INs following treadmill locomotion at low speed (15cm/s, n=3 for each V3 subtype, C); treadmill locomotion at intermediate speed (40cm/s, n=3 for each V3 subtype, D); free swimming (n=3 for each V3 subtype, E); incline treadmill locomotion (+25°, 15cm/s, n=3 for each V3 subtype, F); staggered stepping locomotion (forward speed, 15 cm/s; lateral speed; 7cm/s; n=3 for each V3 subtype, G); and lateral motion without forward stepping (forward speed, 0 cm/s; lateral speed, 7cm/s; n=3 for each V3 subtype, H). (I) Percentage of total c-fos^{+}/Prox1^{+} and c-fos^{+}/Pou2f2^{+} V3 INs (n=3 for each behavioural task and V3 subtype) [ns, not significant; *, p-value <0.05; **, p-value <0.01; ***, p-value <0.001; Mann-Withney-Wilcoxin test, error bars = standard deviation].

Key resources table

REAGENT or RESOURCE	SOURCE	IDENTIFIER
Antibodies		
Alexa Fluor 488-AffiniPure Donkey Anti-Mouse IgG (H+L)	Jackson ImmunoResearch Labs	RRID:AB_2340846
Alexa Fluor 488-AffiniPure Goat Anti-Rat IgG (H+L)	Jackson ImmunoResearch Labs	RRID:AB_2338351
Alexa Fluor® 488 AffiniPure F(ab')$_2$ Fragment Donkey Anti-Guinea Pig IgG (H+L)	Jackson ImmunoResearch Labs	RRID:AB_2617153
Alexa Fluor 488-AffiniPure Donkey Anti-Sheep IgG (H+L)	Jackson ImmunoResearch Labs	RRID:AB_2340745
Donkey Anti-Goat IgG (H+L) Antibody, Alexa Fluor 488 Conjugated	Molecular Probes	RRID:AB_2534102
Alexa Fluor 488-AffiniPure Donkey Anti-Rabbit IgG (H+L)	Jackson ImmunoResearch Labs	RRID:AB_2313584
Alexa Fluor 594-AffiniPure Donkey Anti-Rat IgG (H+L)	Jackson ImmunoResearch Labs	RRID:AB_2340689
Alexa Fluor® 594 AffiniPure Donkey Anti-Rabbit IgG (H+L)	Jackson ImmunoResearch Labs	RRID:AB_2340621
Alexa Fluor 594-AffiniPure Donkey Anti-Goat IgG (H+L)	Jackson ImmunoResearch Labs	RRID:AB_2340433
Alexa Fluor 647 donkey anti-mouse	Jackson ImmunoResearch Labs	RRID:AB_2340863
Alexa Fluor 647-AffiniPure Donkey Anti-Rabbit IgG (H+L)	Jackson ImmunoResearch Labs	RRID:AB_2492288
Cy5-AffiniPure Donkey Anti-Guinea Pig IgG (H+L)	Jackson ImmunoResearch Labs	RRID:AB_2340462
Cy5-AffiniPure Donkey Anti-Sheep IgG (H+L)	Jackson ImmunoResearch Labs	RRID:AB_2340730
Alexa Fluor 647-AffiniPure Donkey Anti-Mouse IgG (H+L)	Jackson ImmunoResearch Labs	RRID:AB_2340863
Mouse Anti-Human ERR gamma Monoclonal Antibody	Actif SCETI	RRID:AB_1964234
Guinea Pig Anti-Olig3	Birchmeier-Kohler Lab	
Recombinant Anti-Oct-2 antibody	Abcam	RRID:AB_2889931
Rabbit Anti-Prox1	Millipore	RRID:AB_177485
PROX1 antibody [5G10]	Abcam	RRID:AB_10563321
BETA 3 (E-17)	Santa Cruz Biotechnology	RRID:AB_2065343
HNF-6 (H-100)	Santa Cruz Biotechnology	RRID:AB_2251852
Human ONECUT2/OC-2 Affinity Purified Polyclonal Ab	R and D Systems	RRID:AB_10640365
Goat Anti-LMO3 Polyclonal Antibody	Santa Cruz Biotechnology	RRID:AB_2136576
Nurr1 (M-196)	Santa Cruz Biotechnology	RRID:AB_2267355
Anti-MAFB antibody produced in rabbit	Sigma-Aldrich	RRID:AB_1079293
Guinea Pig ANTI- Prdm8	Thomas Jessel Lab	CU1791
Guinea Pig ANTI-Otp	Thomas Jessel Lab	CU1497
Guinea Pig ANTI-Foxp1	Thomas Jessel Lab	CU1492
Rat ANTI-Poubf2	Thomas Jessel Lab	CU1796
NR5A2 (C-17)	Santa Cruz Biotechnology	RRID:AB_2154063
Goat Anti-SP8 Polyclonal Antibody	Santa Cruz Biotechnology	RRID:AB_2194626
FOXP2 (N-16)	Santa Cruz Biotechnology	RRID:AB_2107124
Living Colors® DsRed Polyclonal Antibody	Takara Bio	RRID:AB_10013483
anti-tdTomato	SICGEN	RRID:AB_2722750
RFP antibody [5F8]	ChromoTek	RRID:AB_2336064
Mouse ROBO3 Affinity Purified Polyclonal Ab	R and D Systems	RRID:AB_10644167

REAGENT or RESOURCE	SOURCE	IDENTIFIER
Nkx2.2 transcription factor antibody	DSHB	RRID:AB_531794
Bacterial and virus strains		
Biological samples		
Chemicals, peptides, and recombinant proteins		
Lucifer yellow dilithium salt	Thermo Fisher Scientifc	Cat# A-5751, RRID: AB_2536191
Neurobiotin	Vector Laboratories	Cat# SP-1120–20, RRID: AB_2536191
Click-iT® EdU Alexa Fluor® 647 fluorescent labeling	Thermofisher	Cat# ZenC10340
tamoxifen		
5-Ethynyl-2´-deoxyuridine (EdU)	Thermo Fisher Scientific	Cat#: A10044
Critical commercial assays		
Deposited data		
Experimental models: Cell lines		
Experimental models: Organisms/strains		
Sim1^{Cre} mice	Zhang et al, 2008	
NestinFlpoERT2	Lao et al., 2012	
TdTomato Ai14 *B6.Cg-Gt(ROSA)26Sor$^{tm14(CAG0tdTomotato)Hze}$*	The Jackson Laboratory	Jax# 007914
Ai65D *B6;129S-Gt(ROSA)26Sor$^{tm65.1(CAG-tdTomato)Hze/J}$*	The Jackson Laboratory	JAX#021875
Oligonucleotides		
Recombinant DNA		
Software and algorithms		

REAGENT or RESOURCE	SOURCE	IDENTIFIER
pClamp	Molecular Devices	RRID:SCR_011323
ImageJ	ImageJ	RRID:SCR_003070
MATLAB	Mathwork	RRID:SCR_001622
Zen	Zeiss	RRID:SCR_021725
GraphPad Prism	GraphPad	RRID:SCR_002798
Imaris	Bitplane	RRID:SCR_007370
Other		